



## RESEARCH ARTICLE

10.1002/2017JD027234

## Key Points:

- A continuous time-height field of the gradient Richardson number is derived from a suite of remote sensing measurements
- The mixing state of the Arctic boundary layer is diagnosed from the Richardson number; decoupling of cloud from the surface is common
- The surface mixed-layer depth is well characterized by an analytical expression for neutral boundary layer depth

## Correspondence to:

I. M. Brooks  
i.brooks@see.leeds.ac.uk

## Citation:

Brooks, I. M., Tjernström, M., Persson, P. O. G., Shupe, M. D., Atkinson, R. A., ... Brooks, B. J. (2017). The turbulent structure of the Arctic summer boundary layer during The Arctic Summer Cloud-Ocean Study. *Journal of Geophysical Research: Atmospheres*, 122, 9685–9704, <https://doi.org/10.1002/2017JD027234>

Received 6 JUN 2017

Accepted 13 SEP 2017

Accepted article online 22 SEP 2017

Published online 27 SEP 2017

©2017. The Authors.

This is an open access article under the terms of the Creative Commons Attribution License, which permits use, distribution and reproduction in any medium, provided the original work is properly cited.

## The Turbulent Structure of the Arctic Summer Boundary Layer During The Arctic Summer Cloud-Ocean Study

Ian M. Brooks<sup>1</sup> , Michael Tjernström<sup>2</sup> , P. Ola G. Persson<sup>3,4</sup> , Matthew D. Shupe<sup>3,4</sup> , Rebecca A. Atkinson<sup>1</sup>, Guylaine Canut<sup>5</sup>, Cathryn E. Birch<sup>1</sup>, Thorsten Mauritsen<sup>6</sup> , Joseph Sedlar<sup>7</sup>, and Barbara J. Brooks<sup>1,8</sup>

<sup>1</sup>School of Earth and Environment, University of Leeds, Leeds, UK, <sup>2</sup>Department of Meteorology and the Bert Bolin Centre for Climate Research, Stockholm University, Stockholm, Sweden, <sup>3</sup>Cooperative Institute for Research in Environmental Science, University of Colorado Boulder, Boulder, CO, USA, <sup>4</sup>NOAA-ESRL, Boulder, CO, USA, <sup>5</sup>CNRM-GAME (Météo-France and CNRS), Toulouse, France, <sup>6</sup>Max Planck Institute for Meteorology, Hamburg, Germany, <sup>7</sup>Swedish Meteorological and Hydrological Institute, Norrköping, Sweden, <sup>8</sup>National Centre for Atmospheric Science, School of Earth and Environment, University of Leeds, Leeds, UK

**Abstract** The mostly ice covered Arctic Ocean is dominated by low-level liquid- or mixed-phase clouds. Turbulence within stratocumulus is primarily driven by cloud top cooling that induces convective instability. Using a suite of in situ and remote sensing instruments we characterize turbulent mixing in Arctic stratocumulus, and for the first time we estimate profiles of the gradient Richardson number at relatively high resolution in both time (10 min) and altitude (10 m). It is found that the mixing occurs both within the cloud, as expected, and by wind shear instability near the surface. About 75% of the time these two layers are separated by a stably stratified inversion at 100–200 m altitude. Exceptions are associated with low cloud bases that allow the cloud-driven turbulence to reach the surface. The results imply that turbulent coupling between the surface and the cloud is sporadic or intermittent.

**Plain Language Summary** The lower atmosphere over the summertime Arctic Ocean often consists of two well-mixed layers—a surface mixed layer and a cloud mixed layer—that are separated by a weak decoupling layer at about 100 to 300 m above the surface. In these cases, the cloud cannot interact directly with the surface. Large-scale forecast and climate models consistently fail to reproduce this observed structure and may thus fail to correctly reproduce the cloud properties and the amount of energy absorbed by or emitted from the surface as solar and infrared radiation. This contributes to errors in reproducing changes in sea ice concentration over time. Here we use measurements made in the central Arctic to study the processes controlling whether or not the cloud is coupled to the surface. The effect of wind at the surface is found not to be a controlling factor. The depth of the cloud mixed layer is critical, but the multiple processes influencing it cannot be separated using the data available here. However, cooling at cloud top by infrared radiation is key, as is the extension of cloud into the temperature inversion—a unique feature of Arctic clouds.

### 1. Introduction

The central Arctic Ocean, characterized by a surface of semipermanent sea ice, presents unique atmospheric boundary layer (ABL) conditions. During winter the absence of solar radiation allows the formation of a persistent stable boundary layer during cloud-free periods, while low-level clouds tend to force a shallow but relatively well mixed boundary layer (Morrison et al., 2012; Persson et al., 2002; Tjernström & Graversen, 2009). During summer the boundary layer usually has near-neutral stability (Persson et al., 2002; Tjernström et al., 2012) and is commonly capped by stratiform clouds, with a mean cloud fraction as high as 90% (Curry & Ebert, 1992; Liu & Key, 2016; Shupe et al., 2011; Tjernström et al., 2005, 2012; Wang & Key, 2004; Zygmuntowska et al., 2012). Both the clouds and surface fluxes are closely coupled to the structure of the atmospheric boundary layer, being in part controlled by it, and in turn modifying it (Bintanja et al., 2011, 2012; Vihma et al., 2014). These clouds, particularly those containing liquid water, are the dominant control on the surface energy budget (e.g., Shupe & Intrieri, 2004). An intricate balance between their radiative properties at solar and infrared wavelengths and the highly reflecting surface

results in the clouds acting as a warming influence on the surface relative to clear conditions for most of the year (Intrieri et al., 2002; Sedlar et al., 2011; Shupe & Intrieri, 2004), in stark contrast to the effects of similar clouds in other parts of the world. During the summer melt the surface temperature is locked to the melting point of ice despite a strong positive net surface energy flux, and turbulent fluxes do not respond directly to changes in the surface radiative forcing (Persson, 2012). Instead, horizontal advection and clouds have a greater control over the ABL structure (Nilsson, 1996; Tjernström, 2005; Tjernström et al., 2015) which, along with the resulting clouds, forces the surface turbulent and radiative fluxes (Overland, 1985; Persson et al., 2002; Tjernström et al., 2015).

Numerical models for climate and weather forecasting have difficulty representing both the Arctic ABL structure and clouds within it (Birch et al., 2009, 2012; de Boer et al., 2014; Pithan et al., 2014; Sotiropoulou et al., 2016; Tjernström et al., 2008; Wésslen et al., 2014). These difficulties relate directly to an inadequate understanding and representation of processes specific to the Arctic environment, such as long-lived mixed-phase clouds. There are few in situ observations with which to address these issues because of the remote and hostile environment for observational studies. Moreover, because sea ice drifts, is deformed over time, and melts in summer, fixed permanent sites for long-term measurements cannot be established offshore. Consequently, the ensemble of observations forming the empirical basis for the development of reliable parameterizations and testing of models is inadequate.

The ABL vertical structure in summer over sea ice typically presents a near-neutral or weakly stable surface layer, which is often decoupled from a well-mixed cloud layer by a shallow stable layer that suppresses turbulent exchange between the cloud and the surface (Curry, 1986; Curry et al., 2000; Sedlar & Shupe, 2014; Sedlar et al., 2012; Shupe et al., 2013; Sotiropoulou et al., 2014). Shupe et al. (2013) examined estimates of the turbulent kinetic energy (TKE) dissipation rate from Doppler cloud radar, and Sedlar and Shupe (2014) examined thermodynamic profile structure during part of the Arctic Summer Cloud-Ocean Study (ASCOS) (Tjernström et al., 2014) when stratiform cloud capped the boundary layer; both concluded that cloud-surface decoupling occurred about 75% of the time. Sotiropoulou et al. (2014), also using thermodynamic profiles from a longer period of the same field campaign, concluded that clouds were coupled to the surface 28% and decoupled 40% of the time, with the remaining time taken up by a separate class of also decoupled clouds that they termed “stable clouds.”

In this paper we again explore the vertical structure of the late-summer Arctic atmospheric boundary layer during ASCOS. We aim to develop a simple diagnostic for boundary layer mixing state based on profiles of mean quantities and to evaluate the relationships between forcing processes—at the surface and cloud top—and boundary layer structure. We will use observations from a suite of surface-based in situ and remote sensing instruments (Tjernström et al., 2014) deployed over a 3 week period in August 2008 that includes the end of the summer melt and early freeze (Sedlar et al., 2011). ASCOS was designed to study the many interacting processes that govern the properties of Arctic stratiform clouds and link them to the surface, including boundary layer processes. We combine the extensive ground-based remote sensing and in situ measurements to develop a unique continuous time-height Richardson number data set, which is then used, together with radiative transfer modeling also based on the observations, to characterize the boundary layer structure over sea ice. Using this data set, the layering, the turbulent structure, and interactions with clouds and surface fluxes are demonstrated and discussed in a more comprehensive manner than by Shupe et al. (2013) or Sotiropoulou et al. (2014). We compare the observed stability structure with relationships for the surface-forced mixed-layer depths, demonstrating that the surface mixed layer and the cloud mixed layer are separate entities that only intermittently couple to allow deeper mixing, and suggest a mechanism that determines the coupling/decoupling.

## 2. Measurements and Methods

### 2.1. The ASCOS Field Experiment

The ASCOS measurement campaign took place on the Swedish icebreaker *Oden* during the summer of 2008, departing from Svalbard on 2 August and returning on 9 September (Figure 1). While some measurements were conducted throughout the whole cruise, the main observational period took place between 12 August and 1 September, when the *Oden* was moored to a large ice floe at about 87°N,

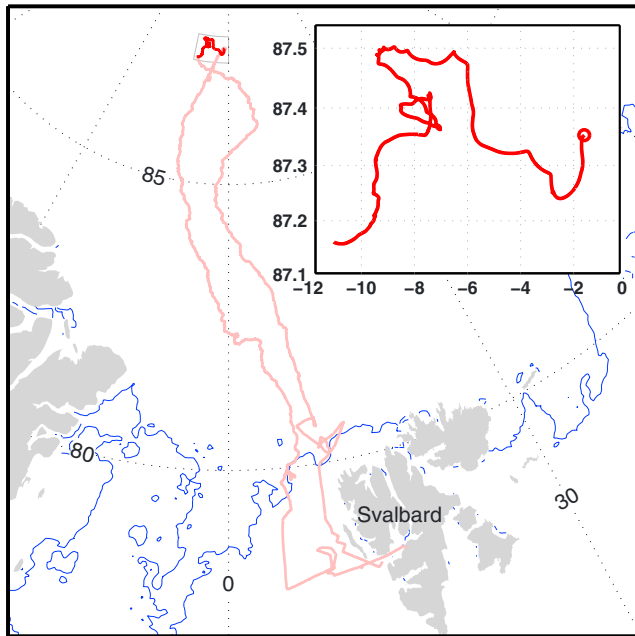


**Figure 1.** The ASCOS cruise track (pink), with the track for the ice drift highlighted in red and shown in detail in the insert. The dashed blue line shows the ice edge on 12 August 2008, at the start of the ASCOS ice drift.

01°W. During the ice drift, an extensive array of instrumentation was deployed on the ice away from the immediate influence of the ship. An overview of the strategy and all instrumentation used during the ASCOS campaign is given by Tjernström et al. (2014); Tjernström et al. (2012) provides a meteorological context and a comparison to earlier summer observations, while Sedlar et al. (2011) describe measurements related to the surface energy budget in detail. Here we give a brief summary of the main instrumentation used in this paper:

1. Radiosoundings of temperature, humidity, and winds were launched every 6 h from the helipad on *Oden*.
2. A tethered balloon system with an instrument package suspended 10 m below was semicontinuously traversing the lowest ~600 m of the atmosphere. The instrumentation consisted of a Gill Windmaster sonic anemometer in an aerodynamic housing with additional sensors for static pressure, mean temperature, and relative humidity, along with control and data logging electronics. The anemometer output turbulent wind components at 10 Hz, which are used to derive power spectra of the turbulent wind components from which TKE dissipation,  $\epsilon$ , is derived.
3. Two masts were erected on the ice approximately 400 m from the ship. A 15 m mast was instrumented with five sonic anemometers for turbulent flux measurements, with Li-COR LI-7500 gas analyzers at two levels to provide high-frequency humidity measurements. The turbulence measurements were supplemented with sensors for measurement of mean temperature and humidity profiles. The turbulence profile was extended with a 30 m mast, instrumented with a single sonic anemometer at the top. All turbulence measurements were made at 20 Hz with fluxes calculated as 10 min averages.
4. A Scintec MFAS phased array Doppler sodar was deployed close to the masts, configured with a vertical resolution of 10 m, a range from 30 to 600 m, and a temporal resolution of 10 min for the wind profiles.
5. A 449 MHz radar wind profiler installed on the *Oden* measured winds from 144 m up to ~3 km at a vertical resolution of 30 m with time averaging over 30 min.
6. An in-house designed 60 GHz scanning microwave radiometer (Westwater et al., 1999), deployed on the starboard bridge-wing roof of *Oden* provided air temperature profiles from 15 m up to 1200 m with a temporal resolution of 5 min. Near the surface the vertical resolution was approximately 10 m, decreasing gradually with altitude to about 200 m at 1 km.
7. A vertically pointing dual-channel (23 and 30 GHz) microwave radiometer (Westwater et al., 2001) provided vertically integrated cloud liquid water path (LWP) and precipitable water vapor.
8. A vertically pointing Ka-band Doppler MilliMeter Cloud Radar (MMCR) sited next to the radar wind profiler on *Oden* measured backscatter intensity and the Doppler velocity spectra from hydrometeors. The MMCR provided information on cloud boundaries and cloud microphysical properties (Shupe et al., 2015).
9. A Vaisala laser ceilometer provided measurements of the cloud base with a vertical resolution of 10 m and 15 s time resolution.

**2.2. Boundary Layer Diagnostics**

Throughout this paper we distinguish between different layers within the boundary layer. For practical reasons, that will become clear below, we will use the term ABL to denote the whole atmospheric boundary layer, extending from the surface up to the base of the main capping inversion, usually near cloud top. The surface mixed layer (SML) will refer to the vertically continuous turbulent layer forced by turbulent fluxes at the surface (note that this is distinct from the “surface layer” of Monin-Obukhov surface layer similarity theory, in which turbulent fluxes are nominally constant), while the cloud mixed layer (CML) refers to the vertically continuous turbulent layer that encompasses the cloud and some part of the subcloud layer. Within the CML we expect turbulence to be driven primarily by buoyant cloud overturning, forced by longwave radiative cooling at or near cloud top, while in the SML turbulence is predominantly wind-shear driven; surface

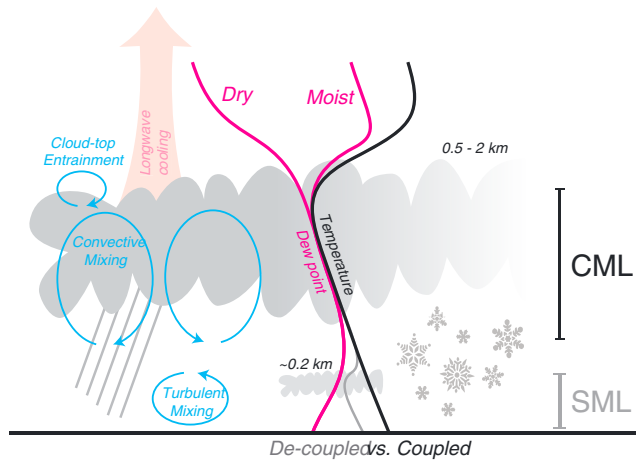


**Figure 2.** Typical summertime stratus-topped Arctic boundary layer and the processes controlling it. The black and gray lines show profiles of temperature for well-mixed and decoupled cases, respectively. The red line shows the profile of specific humidity (inspired by Morrison et al., 2012).

buoyancy fluxes are typically close to zero during the melt season (Birch et al., 2009; Persson et al., 2002; Sedlar et al., 2011). Turbulence may be continuous throughout the whole ABL, as for the prototypical cloud topped ABL, or vertically discontinuous, with the SML and CML separated by a shallow, stable decoupling layer. Figure 2 illustrates the layering of the ABL and the processes controlling it.

Direct measurements of turbulence are available on the micrometeorological masts, up to a height of 30 m, and from the tethered profiler, which extends up to approximately 700 m, but provides only a local measurement along its time-height path. Radar-based retrievals provide continuous profiles of turbulence information, but are only available in atmospheric volumes that contain hydrometeors. In order to obtain continuous estimates of the turbulent structure throughout the full ABL depth we rely upon a remote sensing product: a gradient Richardson number derived from several separate remote sensing retrievals.

**2.2.1. Direct Turbulence Measurements**

There is a strong spectral overlap of the motions of the sonic anemometer hanging under the tethered balloon and the TKE-containing eddies that we have been unable to separate; hence, we were not able to extract eddy-covariance measurements from this system. Instead, we use the turbulent dissipation rate,  $\epsilon$ —the rate at which TKE is dissipated by viscosity at small scales in the atmosphere. The measures of  $\epsilon$  are based on an assumption of stationary well-developed turbulence, with a well-behaved inertial subrange in the power spectra from which  $\epsilon$  can be estimated from Kolmogorov similarity (e.g., Kaimal & Finnigan, 1994). TKE dissipation is usually a good proxy for turbulence intensity, since higher TKE, with larger spectral values at low frequencies, must also mean higher dissipation rate since energy is cascaded down the inertial subrange where the spectral slope is fixed. The tethered balloon  $\epsilon$  estimates are derived from in situ observations and are hence available only at the specific sonde locations, spanning the lowest several hundred meters of the ABL while traversing up and down. These estimates have been compared to continuous profiles of  $\epsilon$  derived from the Doppler radar within cloudy volumes showing good consistency in both magnitude and vertical structure (Shupe et al., 2012).

**2.2.2. Richardson Number**

Before considering the turbulent structure in detail we briefly discuss the methods by which this product is derived from the direct observations. The gradient Richardson number,  $Ri_g$ , provides a measure of the balance between shear and buoyant forces and the resultant turbulent state of the atmosphere, based on mean wind and thermodynamic profiles. Using  $Ri$  to diagnose turbulence is a classical approach; the importance of  $Ri_g$  as an indicator for turbulence is covered in most textbooks on boundary layer turbulence (e.g., Garratt, 1992; Stull, 1988). While a negative  $Ri_g$  is an indication of buoyancy-generated turbulence, positive values are associated with stably stratified turbulence.

The existence of a critical value of  $Ri = Ri_c$ , beyond which turbulence in the atmosphere cannot be sustained, often suggested to be  $Ri_c \sim 0.25$ , has been questioned. Many studies indicate a presence of turbulence at supposedly supercritical values of  $Ri$  (Banta et al., 2003; Gossard et al., 1985; Mauritsen & Svensson, 2007; Rohr et al., 1988; Tjernström et al., 2009). There are also suggestions of a hysteresis, where  $Ri$  in a laminar flow must drop below  $Ri_c \sim 0.25$  to become turbulent, but, once initiated, turbulent flow can remain turbulent to  $Ri_g \sim 1.0$  before becoming again laminar (e.g., Stull, 1988). Other studies imply that other processes, for example, related to gravity waves, can generate and maintain turbulence at supercritical values of  $Ri$  (e.g., Meillier, 2004, 2008, and references therein). The exact values of  $Ri_g$  are also sensitive to the vertical resolution of the mean profiles from which they are derived (Balsley et al., 2008; Tjernström et al., 2009). It should be noted that the classical value of  $Ri_c = 0.25$  was originally derived from linear instability analysis (Miles, 1961) or energy considerations (e.g., Chandrasekhar, 1961), and thus may say very little about nonlinear instabilities and therefore about turbulence. Nevertheless, for simplicity we will in this text generally refer to the regime  $Ri_g > 1$  as nonturbulent, noting that weak sporadic turbulence may occur also here (e.g., Tjernström et al., 2009).

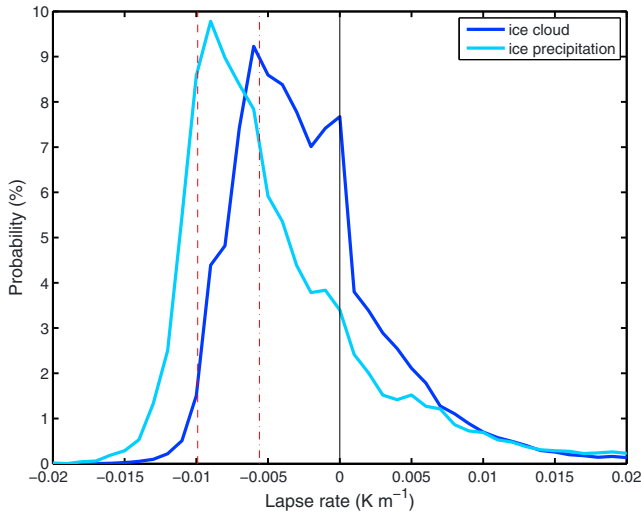


**Figure 3.** Probability distributions of the environmental lapse rate within regions determined by the MMCR cloud radar to be ice only. Also indicated are the dry (red dashed line) and wet (red dot-dashed line) adiabatic lapse rates.

We combine data from multiple remote sensing instruments to derive a continuous Richardson number field from 45 to 1200 m throughout the 3 week ASCOS ice drift period, at 10 m by 10 min resolution. As far as we know, this is the first time such a time-height continuous record of  $Ri_g$  has been derived from remote sensing observations. In a cloud-free environment the traditional gradient Richardson number,  $Ri_g$ , provides a measure of the turbulent conditions:

$$Ri_g = \frac{g}{\theta_v} \frac{\frac{\partial \theta_v}{\partial z}}{\frac{\partial u^2}{\partial z} + \frac{\partial v^2}{\partial z}}, \quad (1a)$$

where  $\theta_v$  is the virtual potential temperature,  $u$  and  $v$  are the zonal and meridional wind components, and  $g$  is gravity. During the Arctic summer near-freezing air temperatures within the ABL mean that the absolute humidity is low; water vapor thus contributes little to the stability structure and may be neglected so that the potential temperature,  $\theta$ , is a good approximation to  $\theta_v$  (Andreas et al., 2005). The dry Richardson number may be represented as

$$Ri_d = \frac{g}{\theta} \frac{(\frac{\partial T}{\partial z} + \Gamma_d)}{\frac{\partial u^2}{\partial z} + \frac{\partial v^2}{\partial z}}, \quad (1b)$$

where  $T$  is the air temperature and  $\Gamma_d$  is the dry adiabatic lapse rate. This is a convenient form here because we have  $T$  profiles from the 60 GHz scanning radiometer, but not high temporal resolution humidity profiles. Within clouds, however, a moist Richardson number,  $Ri_m$ , should be used. Durran and Klemp (1982) define

$$Ri_m = \frac{\frac{g}{T} (\frac{\partial T}{\partial z} + \Gamma_m) \left(1 + \frac{Lq_s}{RT}\right) - \frac{g}{1 + q_w} \frac{\partial q_w}{\partial z}}{\frac{\partial u^2}{\partial z} + \frac{\partial v^2}{\partial z}}, \quad (2)$$

where  $\Gamma_m$  is the moist adiabatic lapse rate,  $q_s$  is the saturation mixing ratio,  $L$  is the latent heat of vaporization, and  $q_w$  is the total water mixing ratio ( $q_w = q_s + q_L$ , where  $q_L$  is the liquid water mixing ratio). The key differences from  $Ri_d$  are the lower value of the moist adiabatic lapse rate and the influence of the vertical gradient in  $q_w$  across cloud top.  $q_L$  was not measured directly but calculated assuming an adiabatic dependence on the temperature profile and constrained by the column-integrated liquid water path derived from the microwave radiometer. This should be a reasonable estimate throughout most of the cloud, although the assumption of adiabatic liquid water content might not be valid close to cloud top due to entrainment and the fact that cloud top was observed to often extend into the temperature inversion (Sedlar et al., 2012).

In order to determine whether  $Ri_d$  or  $Ri_m$  should be used at any given point, cloud phase is first determined from the combined suite of ground-based sensors (Shupe, 2007). We use three categories: clear air, where  $Ri_d$  is appropriate; liquid cloud (or mixed-phase cloud), where  $Ri_m$  is appropriate; and pure ice cloud. In the last category, the appropriate lapse rate to use in equation (2) is not immediately obvious. The ice-only classification encompasses both cloud containing only ice and regions of ice precipitating from mixed-phase clouds. In the former we might expect the lapse rate to be moist adiabatic with respect to ice; within ice precipitation there is no reason to expect a state of adiabatic equilibrium with the surrounding air to be reached. The probability distribution functions (PDFs) of the measured environmental lapse rate within regions flagged as ice only are shown in Figure 3, separated into “ice cloud” and “ice precipitation.” There is a clear difference in behavior, with the lapse-rate PDF within ice clouds peaking around the wet adiabatic lapse rate, while for the lower regions of ice precipitation it peaks much closer to the dry adiabatic lapse rate. Based on this result we use  $Ri_d$  in precipitating ice below cloud and  $Ri_m$  within ice cloud.

The necessary profiles of temperature, liquid water, and wind are all produced by combining measurements from several sensors. The scanning radiometer measures a brightness temperature profile; the retrieval of air temperature requires an initial “guess” as a starting point, provided here by interpolation

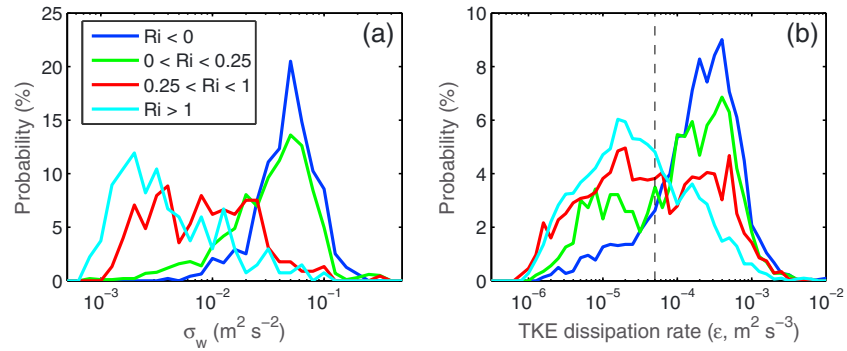


**Figure 4.** Probability distributions of (a) vertical velocity variance,  $\sigma_w^2$ , from a sonic anemometer at 30 m and (b) TKE dissipation rate from the tethered balloon turbulence system, both binned by the  $Ri$  classification.

from the 6-hourly radiosonde profiles. Close to the surface the radiometer adds significant detail to the initial interpolated profile; however, this degrades with altitude, and above approximately 800–1000 m the retrieval differs little from the interpolated radiosonde data. Liquid and ice water concentrations are derived from a combination of measurements from the MMCR, a dual-channel microwave radiometer that provides a column-integrated liquid water path, ceilometers, and radiosondes (Shupe et al., 2015). Wind profiles were obtained from the sodar (30–600 m) and radar wind profiler (200–1200 m).

In order to reduce noise in the temperature and wind gradients both temperature and wind profiles were smoothed with three-point running means in both altitude and time (i.e., 30 m and 30 min, respectively). The different sampling volumes, time bases, measurement principles, and physical separation inevitably introduce discrepancies between the two wind profiling instruments; this makes it difficult to combine the data directly into a single wind field without introducing spurious gradients at the transition between data sets. For this reason, we constructed separate  $Ri$  fields from the two independent wind fields and combined these, prioritizing the sodar-derived values where available, since they are used at the measured resolution while the radar profiler winds are interpolated from a lower resolution onto the desired time-height grid. Below 30 m we calculate  $Ri$  from the temperature and wind profiles measured on the micrometeorological masts. This near-surface record suffers from gaps in the data where icing of the sonic anemometers resulted in degradation or loss of data.

Although there is no strict relationship between  $Ri$  and TKE, confidence in the validity of the classical stability regimes is provided by comparison with more direct measures of turbulent conditions. PDFs of vertical velocity variances from the sonic anemometer at 30 m show very different distributions when binned by the  $Ri$  regime at the lowest level, 55 m (Figure 4a). The peak for the actively turbulent regimes ( $Ri < 0.25$ ) is at approximately  $\sigma_w^2 = 0.05$ , a factor of 25 higher than for the nonturbulent regime ( $Ri > 1$ ), peaking at approximately  $\sigma_w^2 = 0.003$ . For  $0.25 < Ri < 1$  the turbulent state is indeterminate; here the  $\sigma_w^2$  PDF is more uniform than for the other regimes, but somewhat bimodal, spanning almost the full range of values observed with weak peaks for nonturbulent conditions at  $\sigma_w^2 = 0.003$ – $0.004 \text{ m}^2 \text{ s}^{-2}$  and at  $0.02 \text{ m}^2 \text{ s}^{-2}$  corresponding to the low side of the convectively turbulent distribution, reflecting the full range of possible turbulence states.

Similarly, when applying the same type of statistical analysis using  $\epsilon$  derived from the tethered balloon system, interpolating  $Ri$  from the remote sensing profiles to the time and height of the tethered system, a very similar behavior appears (Figure 4b). For  $Ri < 0$  the PDF of  $\epsilon$  has a single peak at  $\sim 4 \times 10^{-4} \text{ m}^2 \text{ s}^{-3}$ , although negatively skewed and much lower values also exist. In the stably stratified but presumably turbulent regime ( $0 < Ri < 0.25$ ), this peak remains, while a secondary peak around  $10^{-5} \text{ m}^2 \text{ s}^{-3}$ , about 40 times lower, appears. In the intermediate range,  $0.25 < Ri < 1.0$  where turbulence might exist, both  $\epsilon$  peaks are about equally strong, while for  $Ri > 1$  the lower peak dominates. Although the shapes of the PDFs are clearly different, the range in  $\epsilon$  values overlap for the extremes,  $Ri < 0$  and  $Ri > 1$ . We suggest that this is a result of either uncertainties in the estimation of  $Ri$  or an imperfect correspondence between TKE, and hence  $\epsilon$ , and  $Ri$ , or both (e.g., Balsley et al., 2008; Tjernström et al., 2009).

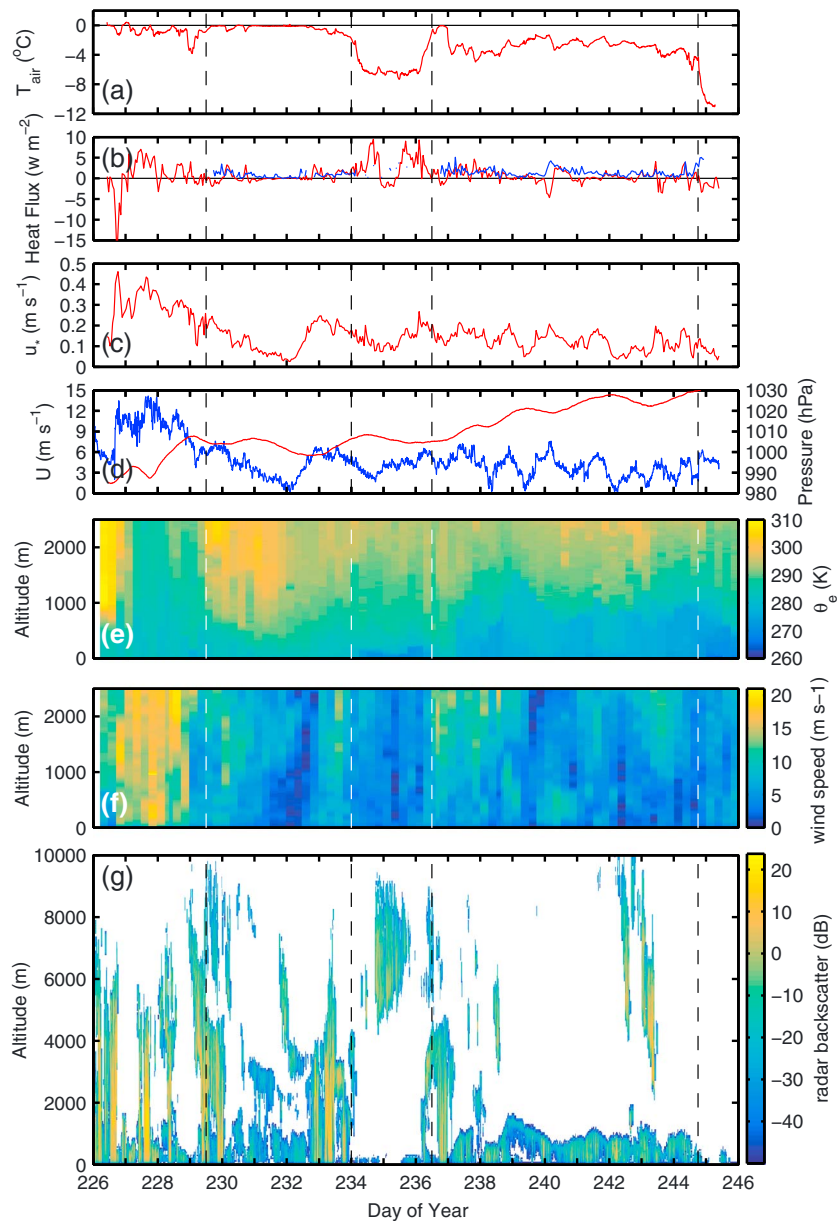


**Figure 5.** Time series of near-surface (a) air temperature ( $^{\circ}\text{C}$ ), (b) sensible (red line) and latent (blue line) turbulent heat fluxes ( $\text{W m}^{-2}$ ), (c) friction velocity,  $u_*$  ( $\text{m s}^{-1}$ ), and (d) wind speed ( $\text{m s}^{-1}$ ) (blue line) and surface pressure (hPa) (red line) and time-height sections of (e) equivalent potential temperature,  $\theta_e$  (K), (f) wind speed ( $\text{m s}^{-1}$ ), and (g) MMCR radar reflectivity (dBZ). The time height sections of  $\theta_e$  and wind speed are derived from radiosoundings. Dashed vertical lines denote the boundaries of meteorological regimes defined in the text.

### 3. The ASCOS Boundary Layer

Before considering the ABL vertical structure from ASCOS in some detail, we will briefly summarize the general meteorological conditions throughout the ice drift. A more extensive description and comparison with previous experiments is given by Tjernström et al. (2012).

The ASCOS ice drift can be divided into distinct time periods with different characteristics (Figure 5). As indicated in Figures 5a, 5b, and 5e, and discussed above and also in Sedlar et al. (2011) and Tjernström et al. (2012), the near surface atmosphere was usually near-neutral, with the surface and overlying air temperatures tracking each other closely. Sedlar et al. (2011) used the surface energy budget observations to determine four distinct periods, while Tjernström et al. (2012) split the first period in two based on the vertical

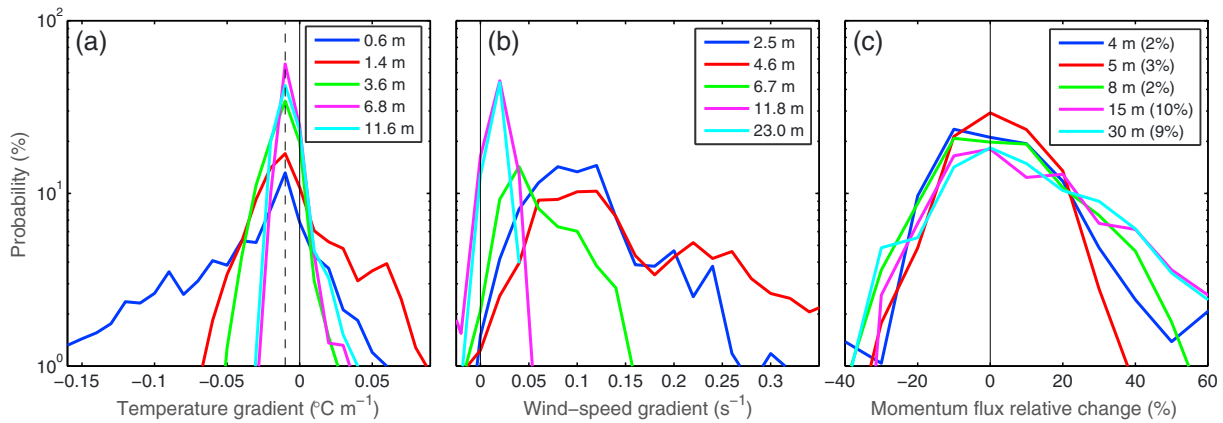


**Figure 6.** Probability statistics of the gradients of (a) temperature ( $^{\circ}\text{C m}^{-1}$ ) and (b) wind speed ( $\text{s}^{-1}$ ) and in (c) the relative change of the friction velocity,  $u^*$  (%), with height, compared with that at the lowest height (0.95 m); the median change is given in the legend. Solid vertical lines indicate zero; in Figure 66a, the dotted vertical line indicates the moist adiabat.

structure of the lower troposphere; these five periods are indicated in Figure 5 with vertical dashed lines. The first two regimes were dominated by the passage of multiple frontal systems with deep, often precipitating, clouds and high wind speeds (Figures 5d and 5g). During both, the mean surface energy budget was positive, allowing melting of ice at the surface (Sedlar et al., 2011); however, the greater synoptic activity during the first regime generated higher variability in the surface temperature, while it remained very close to  $0^{\circ}\text{C}$  during the second period (Figure 5a). Advection of a cold air mass into the region initiated the third regime, in which surface temperature dropped to between  $-4$  and  $-6^{\circ}\text{C}$  (Figure 5a), and melt ponds froze over. Snow fall associated with frontal systems just prior to this, on day of year (DOY) 233, and again on DOY 236, covered the frozen melt ponds. Together with riming on the surface during the colder period this resulted in an irrecoverable increase in albedo, effectively ending the summer melt (Sedlar et al., 2011). The fourth regime was dominated by low-level stratocumulus with few high clouds (Figure 5g) and high pressure with little synoptic activity (Figure 5d). The net surface energy flux remained close to zero while the surface temperature varied between  $-1.2$  and  $-5^{\circ}\text{C}$ , below the melting point of the snow and ice surface but near the freezing point of seawater at  $-1.8^{\circ}\text{C}$ . Hence, radiative forcing of the surface could elicit responses in the turbulent fluxes during this time period (Figure 5b), resulting in modest variability in the near-surface temperature. The fifth regime started with the clearing of the low-level clouds (Figure 5d), strong radiative cooling, and a dramatic drop in temperature to  $-12^{\circ}\text{C}$ ; this was likely the start of the autumn ocean freezeup at this location (Sedlar et al., 2011), although we do not have observations to confirm this since the ice camp ended around midnight between 1 and 2 September (DOY 245–246).

### 3.1. ABL Properties

Figure 6 shows the probability distributions for the temperature and wind speed gradients within the lowest 30 m, from the masts. In this analysis all data were quality checked and only cases with at least three levels of wind speed data and four levels of temperature data available were used; data were also screened to only include times with an unobstructed fetch. The lower quality requirement for the wind speed observations is due to a larger dropout of wind observations from the sonic anemometers, due to icing of the sensor heads, than for temperature. Second-order polynomials in log height were fitted to the remaining profiles and the results quality checked again against the actual observations. As can be seen in Figure 6a, near-surface conditions were most often close to moist neutral; more stable and unstable cases did occur, but rarely and mostly confined to below a few meters. Similarly, significant wind shear (Figure 6b) was mostly confined below 10 m.

Figure 6c shows the relative difference between estimates of friction velocity,  $u_*$ , at each level on the mast and that at the lowest level. Interestingly, there is a trend for slightly higher values with increasing height, apparent in the tail to higher values and higher median values. We believe that this is due to the change in flux footprint with height. Observations at higher levels have a larger footprint and capture the effects of more distant broken-up sea ice, with multiple ice floe edges or ridges in the ice (e.g., Andreas et al.,

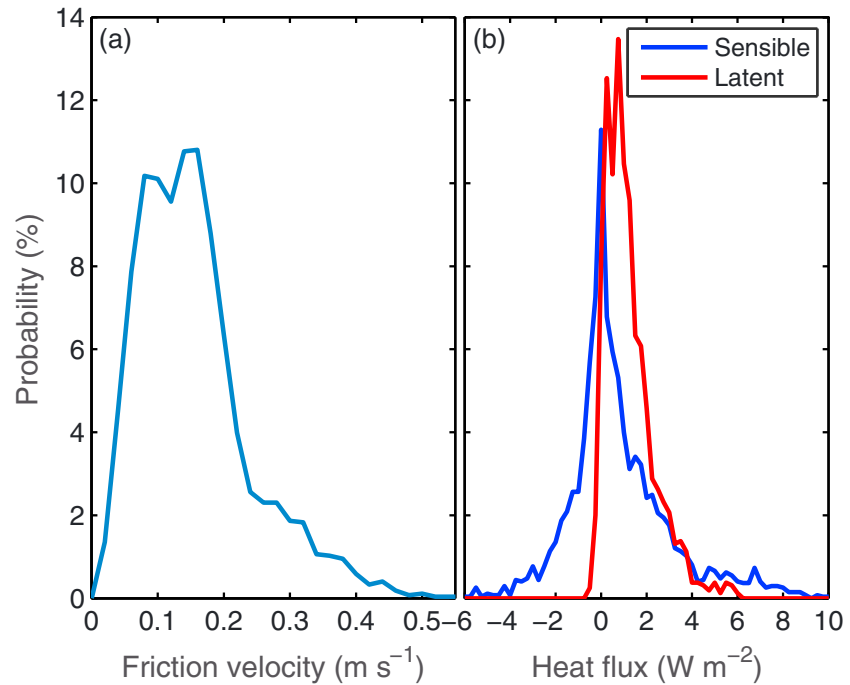


**Figure 7.** Probabilities of the turbulent fluxes: (a) friction velocity ( $\text{m s}^{-1}$ ) and (b) sensible and latent heat fluxes ( $\text{W m}^{-2}$ ).

2010), while the lowest levels only see the local surface conditions around the mast, located on an extensive region of flat, smooth ice. Most of the time these differences are within  $\pm 10\%$  through the lowest 30 m, which allows us to calculate an average surface layer flux for the whole time period (Figure 5), using all available levels in the masts, albeit the number of levels in each average varies with time.

The friction velocity typically fluctuated around  $\sim 0.15 \text{ m s}^{-1}$  (Figure 5c), except during the first few days when the wind was stronger due to a series of passing storms (see Figure 5d). Turbulent sensible and latent heat fluxes (Figure 5b) are defined positive when the flux is upward and were always small ( $< \pm 10 \text{ W m}^{-2}$ ). There are significant gaps in the time series for latent heat flux due to difficulties in keeping the optical surfaces of the instrument clean from frost and snow. Figure 7 shows the PDF for all three turbulent fluxes; the PDF for friction velocity (Figure 7a) peaks around  $0.1 \text{ m s}^{-1}$ , while the sensible heat flux PDF (Figure 7b) is centered on zero, spanning  $\pm 5 \text{ W m}^{-2}$ , and positively skewed with a tail out to  $10 \text{ W m}^{-2}$ . While the latent heat fluxes were mostly positive (evaporation), they were small:  $< 5 \text{ W m}^{-2}$  with the PDF peak at  $\sim 1 \text{ W m}^{-2}$ . Deposition fluxes did occur when the surface temperature fell sufficiently, but these conditions also resulted in frost forming on the LI-7500 optics, contaminating the measurements. These results confirm that the turbulence in the SML is continuous and generated predominantly by wind shear. Different analytical expressions have been suggested to determine the depth of the ABL when lacking continuous turbulence measurements through the whole layer. Historically, the depth of the neutrally stratified SML has often been expressed as

$$H_{\text{SML}} \propto C u_* f^{-1}, \tag{3a}$$

where  $f$  is the Coriolis parameter and the proportionality constant was set to  $C \sim 0.2$  (e.g., Blackadar & Tennekes, 1968). Later, Zilitinkevich (2012) argued that there is a fundamental difference between a “truly neutral” ABL, in which the temperature profile remains neutral to infinity, and a “conventionally neutral” ABL, where the neutral ABL is capped by an inversion, which is the case here. He suggested that these could be estimated as

$$H_{\text{TN}} = 0.6 u_* f^{-1} \tag{3b}$$

and

$$H_{\text{CN}} = 1.36 u_* (fN)^{-1/2}, \tag{3c}$$

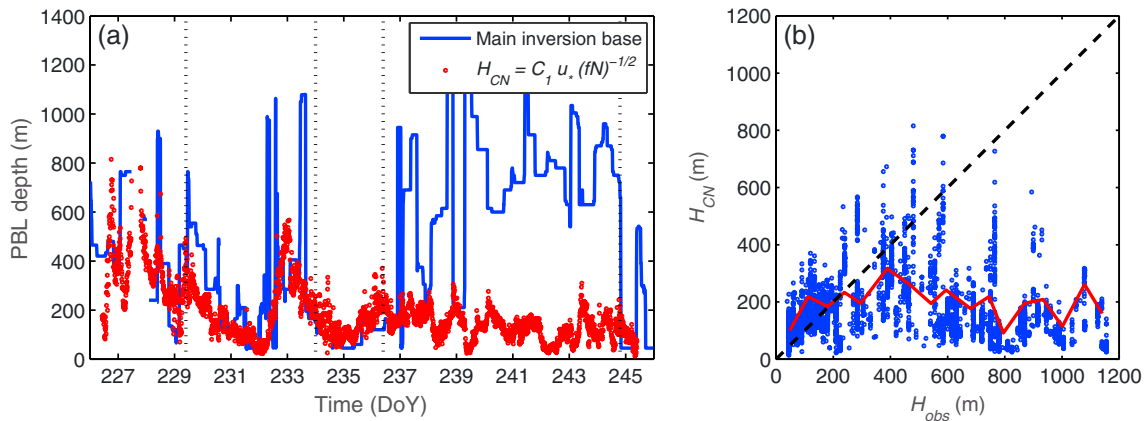


**Figure 8.** Times series of (a) ABL depth from observations ( $H_{obs}$ ; blue solid) and estimated by analytical formulae,  $H_{CN}$  (red dots), and (b) scatterplot comparing  $H_{obs}$  with  $H_{CN}$ , also average relationship (red).

respectively; the constants were determined through large eddy simulation (Zilitinkevich, 2012). In  $H_{CN}$ ,  $N$  is the Brunt-Väisälä frequency across the capping inversion. We can readily calculate all these expressions from the measured friction velocity and the temperature jump across the inversion, and compare to the observed ABL depth ( $H_{obs}$ ), defined here as the height to the main capping inversion base as in Tjernström and Graversen (2009) (see also Tjernström et al., 2012; Sotiropoulou et al., 2014). Note that the inversion is diagnosed from scanning microwave radiometer temperature profiles, with an upper limit at 1200 m; hence, when the main inversion in reality was higher, the algorithm may have picked up a secondary lower inversion.

Figure 8a shows the time series of  $H_{obs}$  and  $H_{CN}$ . Up until ~DOY 237 there is reasonable agreement, although  $H_{obs}$  is sporadically significantly higher than  $H_{CN}$ ; the agreement is especially good for the third period. However, through the fourth and fifth periods there are large differences. This is examined in more detail in Figure 8b. Reasonable agreement is present for shallow ABLs, for depths less than ~200 m,  $H_{CN}$  slightly overestimates the ABL depth; in the range  $200 < z_i < 400$  m,  $H_{CN}$  underestimates ABL depth by ~100 m. However, for  $H_{obs} > 400$  m there is no correlation and  $H_{CN}$  remains at a few hundred meters regardless of  $H_{obs}$ . Clearly, there is sometimes—but not always—a difference between the ABL depth as defined by the main inversion and the SML forced by mechanical TKE production at the surface. This suggests that the turbulent energy generated at the surface is inadequate to mix the atmosphere to the depth suggested by  $H_{obs}$  for these cases. Interestingly,  $H_{SML}$  (using  $C = 0.2$ ) is quite close to  $H_{CN}$  (not shown) for our data, only marginally smaller than  $H_{CN}$ .  $H_{TN}$  (using  $C = 0.6$ ) is a factor of ~3 too large and is not shown in Figure 8. At least for this data, the traditional formulation produces a reasonable result but for the wrong reason, the correspondence possibly being fortuitous. Although it is unclear if this agreement is more general, or specific to this data, this may explain why it has been so successful. The periods of disagreement between the ABL height and  $H_{CN}$  (and  $H_{SML}$ ) are those dominated by low-level stratocumulus clouds (see Figure 5g). This includes the entire fourth period (DOY 237–245) as well as some periods between deeper frontal clouds in period 2 (DOY 230–234). This suggests that the main cloud top inversion is primarily a feature produced by the stratocumulus cloud top cooling and the CML turbulence interacting with features of the large-scale flow, such as subsidence, rather than being a consequence of the forcing from surface friction. In other words, the definition of  $H_{obs}$  as the ABL height using observations is for these cases inconsistent with estimating the ABL depth using  $H_{CN}$  or  $H_{SML}$ . Both primarily come from an estimate of the surface forcing, although  $H_{CN}$  also considers the limiting effects of the inversion stability.  $H_{obs}$  and the ABL depth are hence not always forced entirely from the surface, while  $H_{CN}$  and  $H_{SML}$  are.

### 3.2. Vertical Structure

Figure 9 shows normalized temperature profiles for the entire ASCOS ice drift, about 3 weeks, analyzed from the scanning microwave radiometer. Here the height axis is scaled by the ABL depth  $z_i$ , taken as the base (for near-neutral profiles) or the top (for the stably stratified profiles—surface-based inversions) of the main inversion. The latter are defined as being when the inversion base height is lower than 50 m, the lowest reliable

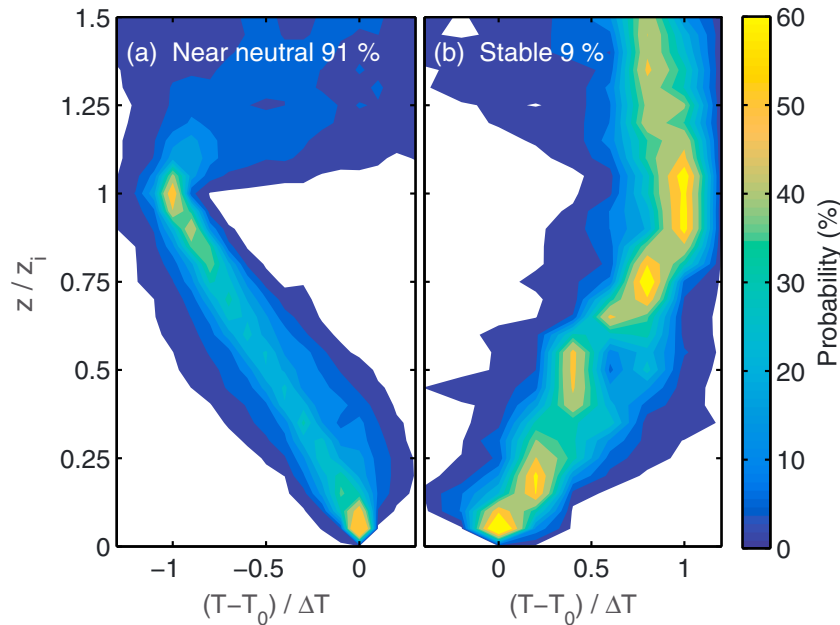


**Figure 9.** Composite profiles of normalized temperature profiles divided in to (a) “near neutral” and (b) “stable,” displayed as probability as a function of altitude. Both axes are scaled with traditional boundary layer scaling; see the text for a discussion. Note that the probability is calculated for each normalized height; hence, summing up the probability each layer will yield 100%.

height for the scanning radiometer. The temperature axis is scaled by subtracting the near-surface temperature,  $T_0$ , from the full temperature profile and dividing by the temperature difference across the ABL,  $\Delta T = (T_{z_i} - T_0)$ .

Stable profiles (i.e., surface-based inversions) occur only 9% of the time, whereas profiles with decreasing temperature with height occur 91% of the time. Although the latter are predominantly linearly decreasing with height, there are cases with a slightly larger stability (less temperature decrease with height) for  $z/z_i < \sim 0.5$ , as indicated by larger probability of scaled temperatures above a linear decrease with height. This indicates that there are cases included with a weak secondary inversion in the lower half of the ABL. For the surface inversions, the stability is generally slightly weaker (less increase with height) in the interval

$0.25 < z/z_i < 0.6$ , giving the curve through the peak probability a slightly s-shaped form. Figure 10 shows the statistics corresponding to the two types of profiles in Figure 9. The bulk stability for the linear profiles is indeed near neutral (Figure 10b, blue line); the temperature difference between ABL top and bottom is most often close to moist adiabatic,  $\sim 0.6^\circ\text{C}$  per 100 m. These ABLs are also most often shallow (PDF peak at  $H = 150$  m) but a substantial number of profiles show ABL depths of over 1 km. Unexpectedly, the stable ABLs (surface inversions) are more often somewhat deeper, with a PDF peak at  $H = 450$  m. The stability varies somewhat uniformly from near zero to  $1.5^\circ\text{C}$  per 100 m; the variability is likely due to the small sample size.

In the absence of continuous direct turbulence observations through the ABL, some information on ABL variability and structure can be gained from analyzing the power spectra of the remote sensing measurements, even though these have limited high-frequency capability. Power spectra are calculated for the time series from each range gate of the scanning radiometer, the sodar, and the wind profiler, and then averaged over height intervals; linear interpolation was used to cover small gaps in the data.

Figure 11a shows the frequency weighted power spectra of temperature from the scanning radiometer; the line at 23 m comes from the ship’s weather station and agrees well with that for the lowest height interval

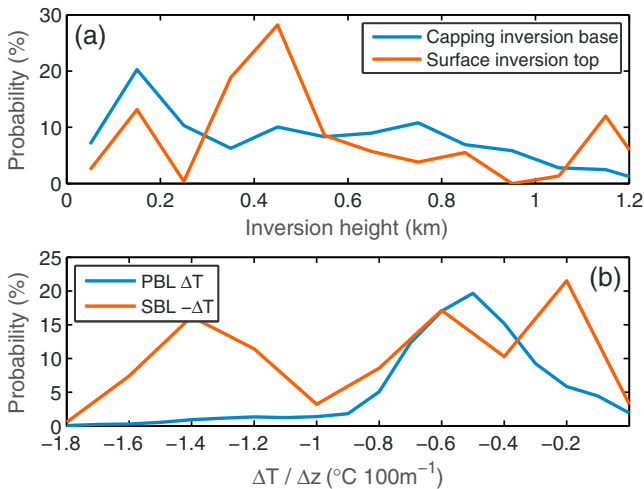


**Figure 10.** Statistics of some properties of the profiles in Figure 9: (a) ABL depth (km) and (b) bulk stability defined as the temperature difference between the ABL top and the surface divided by the ABL depth ( $^\circ\text{C}$  per 100 m); note the reversed sign for the surface-based inversion stability.

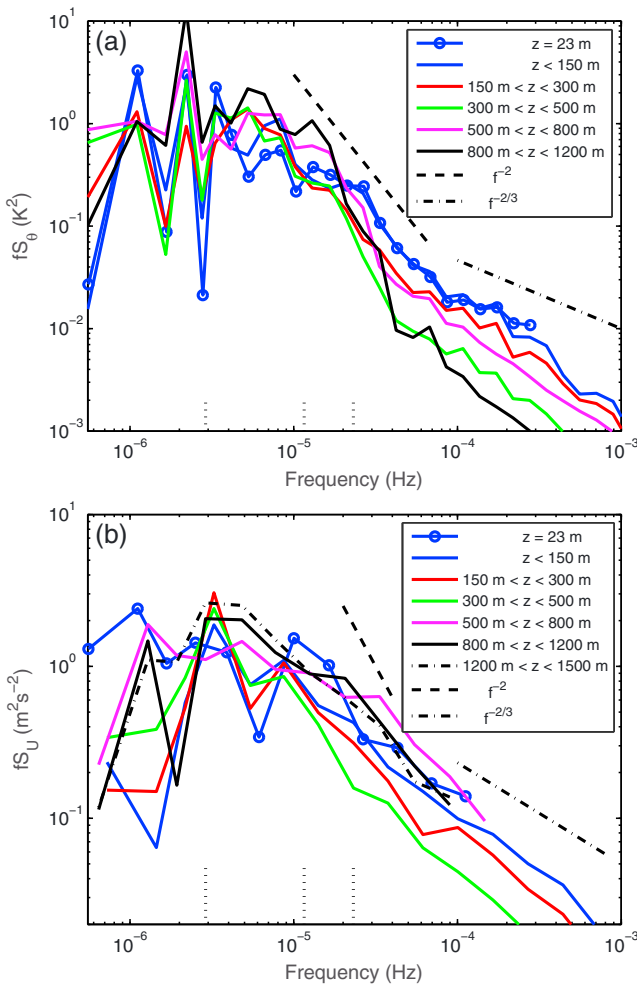


**Figure 11.** Frequency-weighted power spectral density of (a) temperature (K) from the microwave scanning radiometer and (b) scalar wind speed ( $\text{m s}^{-1}$ ) from a combination of sodar and radar wind profilers. Dotted lines on the  $x$  axis correspond to synoptic-scale variability ( $\sim 4$  days;  $2.9 \times 10^{-6}$  Hz), the diurnal period ( $1.15 \times 10^{-5}$  Hz), and the inertial period at  $87^\circ\text{N}$  ( $2.3 \times 10^{-5}$  Hz). Raw spectral estimates are averaged of equal intervals in log frequency, while the black dashed lines show slopes of  $-2$  and  $-2/3$ ; see the text for a discussion.

from the radiometer ( $z < 150$  m). The maximum spectral density occurs in a frequency range corresponding to  $\sim 4$  days, similar to Tjernström (2005), conforming to synoptic-scale variability; the spectral densities are greatest at the highest altitude, within or close to the free troposphere where synoptic-scale variability is expected to dominate. At close to the diurnal frequency the variance initially decreases with altitude, then increases slightly close to the surface; a distinct diurnal cycle in near-surface temperature was observed during the fourth period (Sedlar et al., 2011). For frequencies higher than the diurnal and  $f < \sim 1 \times 10^{-4}$ , the spectral slope adheres to the expected free troposphere slope ( $-2$  in this representation) (Deusebio et al., 2013; Nastrom & Gage, 1985). For all height intervals below 800 m there also seems to be a high-frequency range above  $\sim 1 \times 10^{-4}$  Hz approximating a  $-2/3$  slope, expected for the mesoscale and turbulent scale. Since the sensitivity for this instrument decreases with altitude, especially above  $\sim 800$  m, we expect to see decreasing high-frequency spectral density with altitude; indeed, the highest interval (800–1200 m) has the lowest density. However, for heights below 800 m the spectral density above  $5 \times 10^{-5}$  Hz first decreases with altitude to a minimum for the 300–500 m interval and then increases for the 500–800 m interval; the absolute minimum is at  $\sim 400$  m (not shown). This indicates a separation between turbulence in the lowest and higher layers.

Figure 11b similarly shows the scalar wind speed power spectra using sodar and wind profiler information, below and above 500 m, respectively. The sodar measurements, which have a shorter averaging time, start to develop large gaps in data at higher elevations while the wind profiler has ground clutter problems at lower altitudes; hence, we use the sodar up to 500 m and the wind profiler aloft. An additional layer above 1.2 km is added to capitalize on the larger measurement range of the wind profiler. In general, the temperature variations are smoother than those from the available remote sensing wind information, possibly because of the reduced sensitivity from the scanning radiometer aloft. The peak in the wind speed variance at  $\sim 4$  days is the same as for the temperature spectra, and at levels below 800 m, there is a drop in variance at frequencies just lower than the inertial frequency, forming a local peak close to the inertial frequency. This feature is not present above 800 m. Although there is a less clear  $-2$  slope at frequencies above the inertial, there seems to be a reasonable agreement on a  $-2/3$  slope for  $f > \sim 10^{-4}$ . Again, the spectral density for the high frequencies decreases with height down to  $\sim 300$  m, and then increases again with height; the 300–500 m interval again has the lowest spectral density in the highest frequency range.

Direct observations of turbulence throughout the ABL were only available from the tethered balloon. The maximum altitude was dependent on the dynamic lift from the wind aloft; there are thus more observations in the lower ABL than at the highest elevations and the height is limited to a maximum of about 700 m. Hence, the balloon did not always reach the upper capping inversion. Figure 12a shows the relative probability of turbulent dissipation rate,  $\varepsilon$ , from the tether sonde, as a function of height. In the height interval  $\sim 100$  m to  $\sim 400$  m, the PDF is clearly bimodal. In order to separate turbulent from nonturbulent flows we set a threshold dissipation rate of  $\varepsilon \sim 5 \times 10^{-5} \text{ m}^2 \text{ s}^{-3}$ ; this empirical value is chosen based on inspection of the  $\varepsilon$  and  $\theta$  profiles across the inversion base, effectively separating well-mixed (turbulent) from stable (nonturbulent) portions of the profile. Over 50% of the observations in the 100–400 m interval would by this definition be nonturbulent, again suggesting an intermittent decoupling between the SML and the CML. Normalizing the altitudes with the observed ABL depth, as defined earlier, merges the two regimes (Figure 12b); clearly, this scaling is not appropriate to describe the vertical structure of this ABL. Still, a separation emerges between the maximum probability of  $\varepsilon$  values below  $z/z_i \sim 0.2$  and a separate maximum for  $0.4 < z/z_i < 0.8$ , illustrating the turbulence layering.

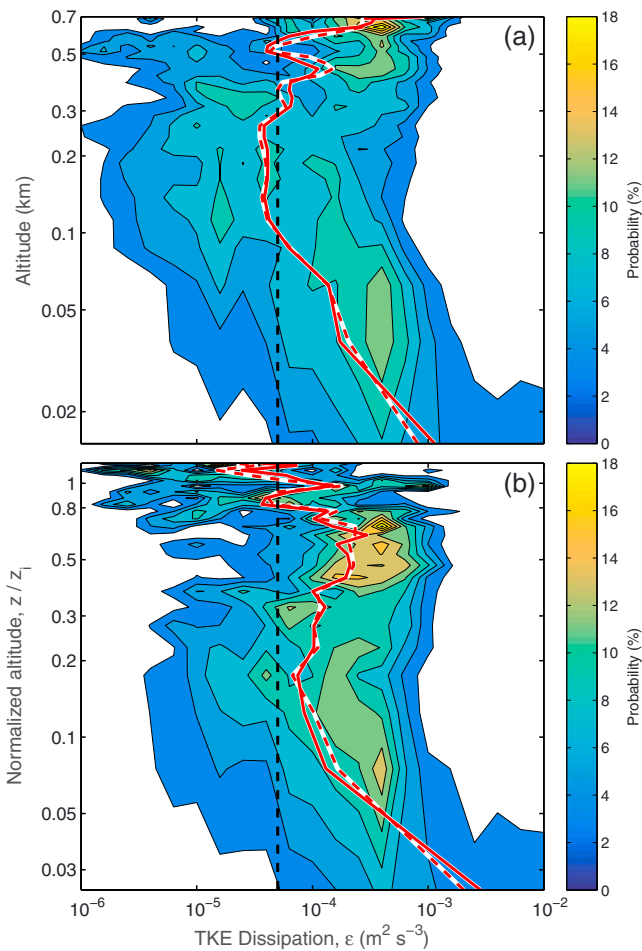


**Figure 12.** Probability (%) of the TKE dissipation rate,  $\epsilon$  ( $\text{m}^2 \text{s}^{-3}$ ), at each level from the tethered balloon (a) as a function of height and (b) as a function of height scaled by ABL depth ( $H_{\text{obs}}$ ). The dashed vertical line at  $\epsilon = 5 \times 10^{-5} \text{m}^2 \text{s}^{-3}$  indicates the threshold between turbulent and nonturbulent conditions. The solid red and dashed red and white lines are the mean and median profiles, respectively.

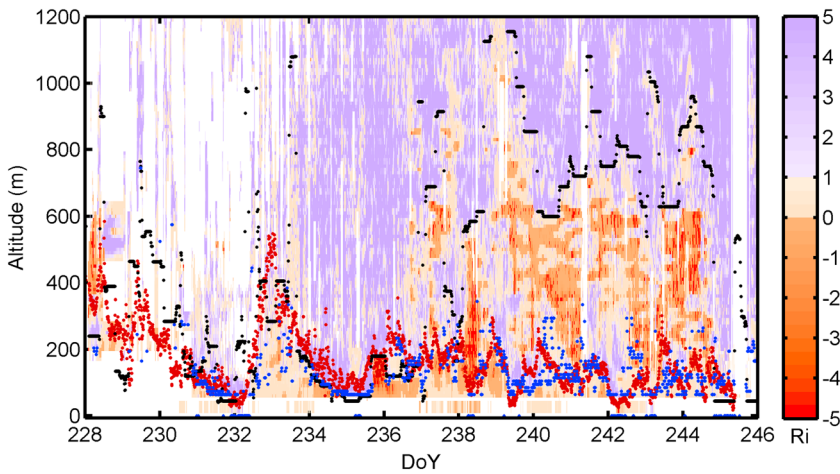
In section 2.2.2, we described the development of a Richardson number data set that might provide a means to delineate periods of coupling from those of no coupling between the cloud layer and the surface, and also to analyze the statistics of these layers. Figure 13 shows the  $Ri$  time-height cross section, limiting the scale to  $-5 < Ri < 5$ . The result is noisy, primarily as a consequence of having the wind speed gradient squared in the denominator; this gradient is quite variable and difficult to estimate, especially when it becomes small. There are also substantial height and time intervals where  $Ri$  could not be determined because of gaps in the wind profile data, particularly in the first 5 days when multiple frontal systems passed through. Still, one can see a general behavior, with higher  $Ri$  aloft, and low values at the surface. An indication of decoupling can also be seen from DOY 237–245, with a layer of high  $Ri$  below 400 m and lower  $Ri$  aloft. The ABL depth; the analytical expression for SML depth,  $H_{CN}$ ; and a measure of the SML depth derived from the Richardson number,  $H_{Ri}$  are also shown;  $H_{Ri}$  is defined as the lowest nonturbulent ( $Ri \geq 1$ ) level.  $H_{CN}$  generally follows  $H_{Ri}$  closely, and during the first half of the time series both are also in generally good agreement with the ABL depth (see also Figure 8a); however, the decoupling nature of the ABL becomes quite clear from DOY ~237 onward, where the ABL depth becomes substantially larger than  $H_{CN}$  and  $H_{Ri}$ , explaining the differences between the analyzed ABL depth from the temperature profiles and the analytical formulas in Figure 8. Note also how the ABL depth tightly follows the upper limit for subcritical  $Ri$ .

### 3.3. Radiation and Vertical Turbulent Structure

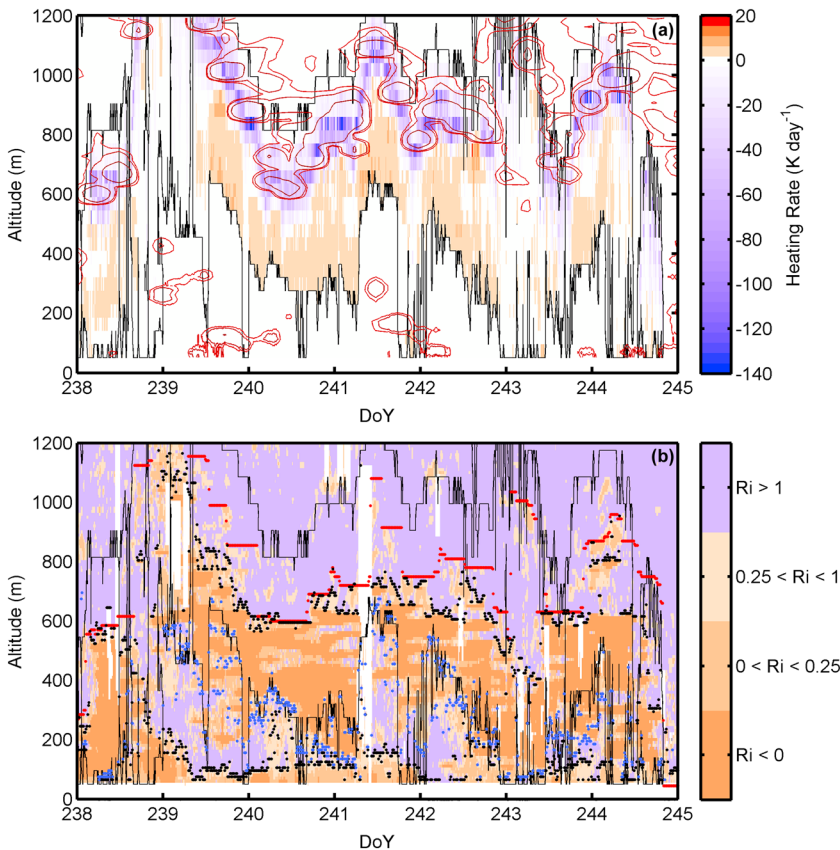
Before analyzing the  $Ri$  data set more closely, we first investigate the correspondence between the turbulence structure of the boundary layer and radiative forcing using a radiative transfer model—the Edwards-Slingo radiative transfer code (Edwards & Slingo, 1996). This is the same scheme used by the Met Office Unified Model (Ingram et al., 1997) and provides profiles of the radiative heating/cooling rates. The model was run with input profiles of the observed atmospheric thermodynamic structure from radiosondes and scanning radiometer, and cloud properties from remote sensing retrievals (Shupe et al., 2015) at 10 min intervals. We restrict our analysis here to the fourth regime—the stratocumulus period from DOY 238 to DOY 245 (Sedlar et al., 2011) when decoupling between the SML and CML was clearly occurring (see Figure 12).

Figure 14a shows the total net radiative heating rate along with cloud boundaries (liquid water content (LWC) = 0) and contours of the vertical temperature gradient. Cloud extends 100–300 m into the inversion, which has been frequently observed over the summer Arctic (Sedlar, 2014; Sedlar et al., 2012), and the majority of cloud top cooling is located within the inversion layer and thus mostly above the ABL top. Below, there is weak radiative heating, typically  $< 5 \text{K d}^{-1}$ , an order of magnitude smaller than the cooling at the cloud top. A caveat here is that the Shupe et al. (2015) retrieval assumes an adiabatic LWC profile, constrained by the LWP. In a well-mixed cloud this is a reasonable assumption, but might not hold in the stable inversion layer. The effects on the radiative cooling at cloud top by assumptions of the LWC profile where cloud extends into the inversion were investigated by Sedlar et al. (2012). They concluded that the longwave cooling was indeed shifted up into the inversion layer. The peak cooling rate was weakened relative to that from a similar cloud layer with a top capped by the inversion base, although by less than a factor of 2, and cooling was typically also spread over a greater vertical range.

Figure 14b shows  $Ri$  along with the ABL top and cloud boundaries and SML and CML boundaries derived from  $Ri$  profiles (see section 3.4 for definitions). For clarity,  $Ri$  has here been binned into four ranges bounded by the critical values. The cloud mixed layer—the more or less continuously turbulent region originating within cloud—extends from the ABL top (or some level below it) to below cloud base. Note



**Figure 13.** Time-height cross section of Richardson number. Data below 35 m derive from the mast profiles. Also included are the SML depth from the analytical formula  $H_{CN} = 1.36 u_* (fN)^{-1/2}$  (red dots), SML depths from an analysis of  $Ri$  ( $H_{Ri}$ ; blue dots), and observed ABL depths ( $z_i$ ; black dots). The color scale is broken at  $Ri = 0$  and  $Ri = 1$  to make distinct the regimes of turbulent convection, stratified nonturbulent flow, and stable but turbulent (or potentially turbulent) flow.



**Figure 14.** Time-height cross sections of (a) total radiative heating ( $K d^{-1}$ ), cloud boundaries ( $LWC = 0 g kg^{-1}$ ; black line), contours of vertical temperature gradient,  $dT/dz$  ( $+0.005, +0.01, +0.03 K m^{-1}$ ; red lines), and (b) Richardson number binned into ranges between critical values for clarity, with cloud boundaries ( $LWC = 0$ , black line), ABL top (red dots), CML and SML top (black dots), and CML base (blue dots).

that the significant portion of the cloud that extends into the inversion, and where the majority of longwave cooling is located, is nonturbulent. There are also regions of nonturbulent flow below cloud whenever cloud base lies above about 100–200 m, indicating that decoupling occurs primarily when clouds are sufficiently high above the surface (Shupe et al., 2013; Sotiropoulou et al., 2014).

Longwave cooling at cloud top is largely confined to a layer above the level at which the liquid water path, integrated down from cloud top, is sufficient for the cloud to be effectively a blackbody in the infrared, about  $30\text{--}50 g m^{-2}$  (e.g., Stephens, 1978). The extension of Arctic stratus cloud into the inversion means that this cooling layer lies mostly within the inversion; the strong stability in this layer limits the generation of turbulence by the downward convection of cooled air such that the radiative cooling instead partly drives condensation (Sedlar & Shupe, 2014; Shupe et al., 2013). The upper cloud is thus only weakly and perhaps intermittently turbulent. Figure 14b shows this layer to mostly have  $Ri > 1$ , with intermittent patches of  $Ri < 1$ , and occasionally  $Ri < 0$ . A convectively driven fully turbulent layer typically starts at or some distance below the inversion base and extends down to below cloud base. Weaker turbulence within the body of the cloud, compared to what is expected in typical subtropical marine stratocumulus, means that the depth of the turbulent layer that can be maintained is also limited. At the surface turbulence is primarily mechanically generated and conditions are almost always close to neutral. The turbulent layer is thus of limited extent, roughly corresponding to the depth of the conventionally neutral layer depth,  $H_{CN}$ . Continuous turbulence is maintained throughout the ABL, from the surface through cloud, if the two mixed layers overlap. If the cloud is at a sufficiently high altitude, then the CML base does not reach the top of the SML, the ABL is decoupled, and a layer with no or very limited turbulence exists between the top of the SML and the base of the CML.

### 3.4. Boundary Layer Coupling Statistics

Although noisy, the  $Ri$  data set allows a more stringent analysis of the ABL layering during ASCOS than the direct in situ measurements. We define several boundaries between turbulent and nonturbulent layers from the  $Ri$  time-height cross section as follows: the upper limit of the SML is taken as  $H_{Ri}$ ; it is undefined if the lowest data bin is nonturbulent, for example, in the presence of a surface-based inversion. The upper limit of the CML is the lowest nonturbulent level ( $Ri \geq 1$ ) within cloud that is above the highest level where conditions are convective ( $Ri < 0$ ). The CML base is only defined if SML top is

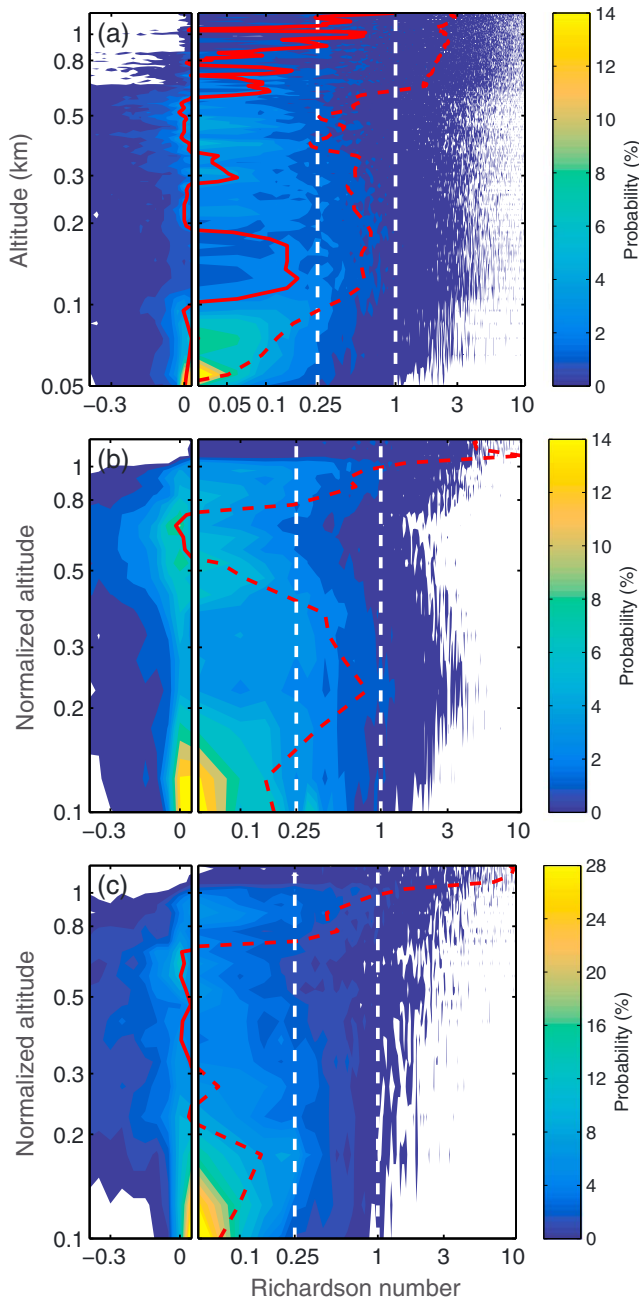


**Figure 15.** Probability (%) of values of  $Ri$  at each altitude as a function of (a) height and using height normalized by the ABL depth ( $H_{obs}$ ) for (b) all decoupled profiles and (c) all coupled profiles. Also shown in Figure 15a is the PDF peak (solid red) and the median (dashed red) and in Figures 15b and 15c the median (dashed red) profiles. Note that the probability is calculated for each layer; hence, summing up the probability across all values of  $Ri$  for each layer will yield 100%.

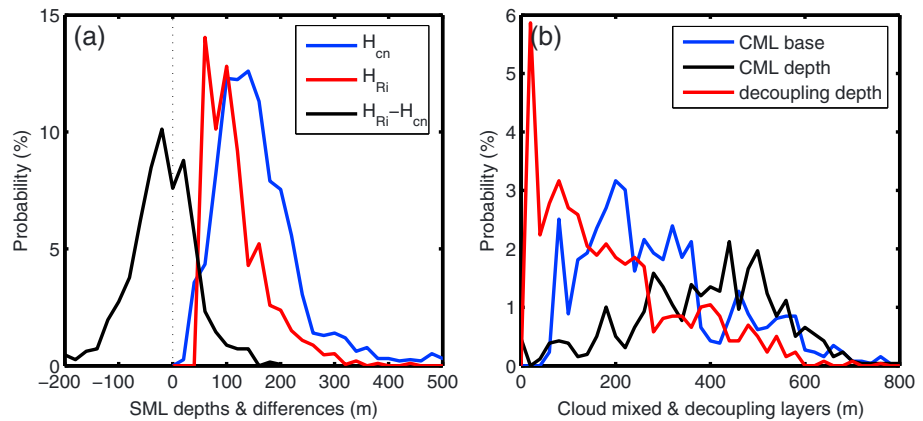
defined, and is then the highest nonturbulent level ( $Ri \geq 1$ ) that is both above SML top and below cloud base.

Figure 15 shows the statistical distribution of  $Ri$  for the whole data set, as a function of altitude. Note that with the true height axis (Figure 15a), the statistics are smeared over height since the capping inversion ranges between  $\sim 100$  m and  $>1$  km; decoupling is not always present, and when it is, it appears at different height intervals, usually starting in the lowest 100–200 m but with a varying depth. The PDFs are strongly skewed, as can be seen by comparing the PDF peak values (solid red) to the median value (dashed red). There are a high percentage of cases having  $Ri < 0.25$  below about 100 m, and again between 200 m and 600 m. There is a distinct shift in the PDF toward larger values of  $Ri$  between roughly 100 m and 300 m, especially below 200 m, note the decrease in the median values around 300–400 m. The largest median values ( $Ri \sim 0.5$ ) are found for heights of 100–300 m, indicating the typical range for, and most common level of decoupling.

Figures 15b and 15c show the distribution when scaling the height axis with  $H_{obs}$ , for decoupled profiles and coupled profiles separately. Note that  $H_{obs}$  might still be substantially deeper than  $H_{CN}$  in the coupled case; this simply means that the CML base is low enough to reach down into the SML. Although the peak of the (very skewed) PDFs for the decoupled cases (Figure 15b) remains close to zero throughout the ABL depth, most decoupled profiles display  $Ri < 0.25$  below  $z/z_i \sim 0.2$ . In the height interval  $\sim 0.2 < z/z_i < \sim 0.5$  the PDFs of  $Ri$  becomes very wide; median values of  $Ri > 0.25$  occur up to  $z/z_i < \sim 0.4$ . For  $\sim 0.5 < z/z_i < \sim 0.7$ , the median  $Ri$  is negative, indicative of the strong convective mixing in the CML. Although the median  $Ri$  increases fast aloft the peak of the PDF remains close to zero up to the ABL top at  $z/z_i \sim 1.0$ . The coupled profiles (Figure 15c) display more narrow PDFs through the entire ABL, with higher relative probabilities close to zero (note the doubling of the color scale in Figure 15c). A majority of all profiles has  $Ri$  close to zero below  $z/z_i \sim 0.2$ , as in Figure 15b, but the PDFs then remain narrow up through the ABL with a median profile close to zero all the way to  $z/z_i < \sim 0.7$ ; aloft the behavior is similar in both cases. There is a slight maximum in the PDFs in the  $\sim 0.5 < z/z_i < \sim 0.7$  height interval; these PDFs are similar to those in Figure 15b in the same height interval but appear less prominent in this representation when compared to the higher probabilities for  $z/z_i < \sim 0.2$ . Hence, some coupled profiles may also feature a CML, although it is not strictly separated from the SML, while some coupled profiles do not have a well-defined CML at all.

We examine the statistics of the surface and cloud mixed layers in Figure 16. In Figure 16a, only cases where the SML is defined are considered. The absolute peak of the PDF for the  $Ri$ -based SML depth,  $H_{Ri}$  is at 65 m, the lowest value possible, imposed by the lower limits of the sodar and radiometer data; there is a broad peak up to  $\sim 100$  m and then probability decreases relatively uniformly to about 200 m with a tail out to

about 400 m. The  $H_{Ri}$  distribution can be compared with the Zilitinkevich (2012) expression for the capped neutral layer depth,  $H_{CN}$ ; this PDF of course does have values lower than 65 m but peaks more uniformly and slightly higher, at 100–150 m, and with a longer tail at higher values. If all  $H_{CN}$  values below 65 m are set to that value, mimicking the lower limit in the  $Ri$  data, that PDF also has a main peak at 65 m. The PDF for the difference between the two estimates ( $H_{Ri} - H_{CN}$ ) has an absolute peak at  $-20$  m, but with a broader peak centered just below zero; if the values below 65 m in the analytical estimate are replaced by 65 m,



**Figure 16.** Probability of (a) SML depths from the  $Ri$  analysis,  $H_{Ri}$ , and the analytical formula,  $H_{CN}$ , and their difference and (b) of the CML base height, CML depth, and the decoupling layer depth (CML base–SML top), all derived from  $Ri$ .

the peak of the difference PDF is shifted closer to zero. Moreover, the time series of the two follow each other closely (Figure 13).

The CML base (Figure 16b) has a relatively flat, broad peak in the distribution from 80 m to 360 m with an absolute peak at 200 m and a tail extending up to almost 800 m. The CML depth has a very broad distribution, peaking around 400–500 m. The depth of the decoupled layer (CML base–SML top) has a highly skewed distribution, peaking at the lowest possible value or 10 m, and decreasing relatively smoothly to about 600 m. Shupe et al. (2013) presented a similar PDF for CML depth, derived from Doppler cloud radar measurements during 24–31 August (DOY 237–244), with a slightly bimodal character with peaks at 500 m and 680 m; our results agree very well with the lower dominating mode of their PDF. However, their analysis also includes periods when the cloud top was above 1.2 km, which is the maximum height in the present  $Ri$  data set. The most common depth of the decoupling layer found here is 10 m, one vertical grid increment. This is not the same as saying that marginal coupling is the most common occurrence; in fact, defining decoupling as when the decoupling layer is deeper than 20 m, decoupling occurs 48% of the time for the whole data set and 76% of the time for the stratocumulus period. This is in close agreement with 75% quoted by Shupe et al. (2013) and Sedlar and Shupe (2014) for the stratocumulus period, using an entirely different technique, and with 72% in Sotiropoulou et al. (2014) (decoupled plus stable clouds), using yet another independent technique and a longer data set.

A caveat to the statistics of layer boundaries is that there is considerable noise in the  $Ri$  profiles, with multiple very shallow turbulent/nonturbulent layers embedded within deeper layers of nonturbulent/turbulent conditions. While details of the individual boundary heights and layer depths change if selection criteria are modified or the  $Ri$  field is smoothed, the fraction of time that decoupling is found to occur is almost unchanged, and none of our conclusions are affected.

#### 4. Conclusion

Using a multisensor approach, the vertical structure of the Arctic ABL from the ASCOS 3 week ice drift was analyzed. A key component in the analysis was a unique  $Ri$  number data set with high spatial and temporal resolution, developed using a suite of remote sensors. These provided temperature profiles from a scanning radiometer, cloud properties from a combination of Doppler cloud radar, ceilometer and a dual-wavelength microwave radiometer, and wind speed profiles from a Doppler sodar and 449 MHz wind profiling radar. The  $Ri$  number data set has been qualitatively evaluated against eddy covariance turbulence measurements from a sonic anemometer on a 30 m mast and against TKE dissipation rates estimated from a tethered balloon-based sonic anemometer and derived from a ground-based Doppler radar, with encouraging consistency. As far as the authors are aware, such a continuous time-and-height resolved  $Ri$  number data set from remote sensing measurements has not previously been presented. Throughout this study, the ABL was defined as the whole layer from the surface up to the main capping inversion, as determined by temperature profiles from a

scanning microwave radiometer (and denoted  $H_{\text{obs}}$  during comparisons with other measures of boundary layer depth). The ABL is subdivided into a surface mixed layer (SML), a decoupling layer, and a cloud mixed layer (CML). Profiles of TKE dissipation observations support this presence of a multilayer structure of the ABL. Using the  $Ri$  number data set, the statistics for the different layers within the ABL have been analyzed. The main conclusions are the following:

1. The bulk static stability of the ASCOS ABL was stable ~9% of the time; the remaining 91% of the time the ABL was nearly moist neutrally stratified, capped by a stable temperature inversion.
2. Surface turbulent heat fluxes were generally quite small and the turbulence in the lower ABL was predominantly shear driven. The thickness of the ABL was most often only a few hundred meters, but was sometimes significantly deeper, up to ~1 km or more. The deeper ABLs were generally associated with low-level stratocumulus clouds.
3. Power spectra of temperature and scalar wind speed from remote sensors and TKE dissipation profiles from the tethered balloon system suggest a mid-ABL region that was sometimes nonturbulent, here denoted the decoupling layer. The decoupling is confirmed by the  $Ri$  number data; the latter suggests that that decoupling occurs about 48% of the time during the ASCOS ice drift and 76% of the time during the 7 day stratocumulus period, in good agreement with the results from other ASCOS studies using different techniques.
4. An analytical expression for boundary layer depth based on friction velocity, the Coriolis parameter, and the stability of the ABL-capping inversion (equation (3c)) provides a reasonable estimate for the ABL depth when it corresponds to the SML depth. It severely underestimates the ABL depth and appears uncorrelated to it when the ABL corresponds with the CML top. Thus, the surface wind stress is not directly correlated with the observed coupling/decoupling state but does determine the depth of the surface mixed layer when the BL is decoupled. A change in wind stress might thus also promote a change in coupling state.
5. The decoupling layer for the stratocumulus period, as analyzed from the  $Ri$  number data set, is most often <250 m deep but occasionally up to 600 m, while the CML depth was typically 300–600 m, most often 400–500 m. The CML top was generally several hundred meters below cloud top, and the CML base usually extended below cloud base.  $Ri$  is most often negative within the CML, indicating buoyant cloud overturning forced by longwave radiative cooling near cloud top.

This gives a detailed picture of the typical structure of the summertime stratus-topped Arctic boundary layer and the processes controlling it that were illustrated schematically in Figure 2.

Coupling or decoupling of the cloud layer from the surface depends upon whether or not the two independently driven mixed layers—the surface mixed layer and the cloud mixed layer—meet or not. Here the surface mixed layer is near neutral and driven primarily by mechanically generated turbulence at the surface; its depth thus depends on wind speed and surface roughness. The latter can vary substantially over a wide range of spatial scales, depending on ice fraction and the physical properties of the sea ice (e.g., Elvidge et al., 2016; Held et al., 2011). Stable surface stratification would decrease the surface mixed layer depth or result in a surface-based inversion, while unstable conditions would likely ensure coupling with the cloud. The cloud mixed layer is driven by buoyant sinking of air cooled near cloud top by longwave radiation. The strength of turbulence will depend on the net radiative cooling near cloud top, in turn dependent upon the temperature of cloud top, downwelling longwave radiation from the overlying atmosphere and any higher level clouds, and downwelling solar radiation; the extent to which cloud top extends into the inversion; and the temperature gradient within the inversion. The presence and strength of a humidity inversion will also impact turbulence intensity through its influence on how much of the radiative cooling drives condensation rather than buoyant convection. The balance between liquid and ice water in the cloud will affect latent heat processes and thus net heating or cooling in regions of condensation or evaporation. Most of these factors are interlinked, and untangling their independent influences on the mixed layer depth is difficult with limited observational data. Some relationships have, however, been identified. The ASCOS data show positive correlations between CML depth and turbulence intensity in cloud, cloud depth, cloud top height, and liquid water path (Shupe et al., 2013), although these are not necessarily independent of each other. Large eddy simulation has shown that the presence of a humidity inversion reduces turbulence in cloud (Solomon et al., 2014), slowing growth of the CML. Further large eddy simulation studies are required to fully understand the detailed interplay between the properties of the humidity inversion, the extension of cloud into the inversion, and the radiatively forced turbulence controlling the CML depth.

Decoupling of the cloud layer from the surface essentially means that there is no moisture flux from the surface available to the cloud layer and that aerosols, if generated at the surface, cannot be transported to reach the cloud layer (e.g., Shupe et al., 2013). These vertical transports can therefore only occur when the SML is coupled with the CML—about half the time from this limited, late-summer data set, but significantly less frequently for the stratocumulus cloud periods. Since some weak precipitation was observed most of the time (Tjernström et al., 2012) another source of moisture must be present to replenish the cloud layer or it would gradually dissipate. Hence, it has been speculated and demonstrated with large eddy simulations that moisture inversions, where the absolute humidity increases across cloud top (Sedlar, 2014; Sedlar et al., 2012), could be a source of moisture (Solomon et al., 2011). Large eddy simulation studies suggest that a humidity inversion can provide sufficient moisture to maintain long-lived Arctic stratus clouds that are decoupled from the surface (Solomon et al., 2014). Moisture inversions are likely dependent on long-range transport of air from beyond the ice cap, which means that it could also provide advected aerosols (Igel et al., 2017; Shupe et al., 2013). This structure also means that in situ observations at, or near, the surface provide very little information on the properties of the cloud layer when the SML and CML are decoupled.

These results are, however, based on only 3 weeks of measurements, in some cases even less, and there is very little similar data to compare to; consequently, the representativity of these results can always be questioned and the only remedy is to obtain more observations. The *Ri* analysis during ASCOS was made possible by deploying some instruments on the ice, for example, the Doppler sodar and the turbulence observations on the masts. This required a dedicated expedition, since the icebreaker had to remain stationary for a long time. However, the fact that the *Ri* number data set could be based mainly on remote sensing instruments opens up possibilities to provide the vertical turbulence structure using only observations made on board. The lower level winds here came from the sodar; this is not practical on a ship because of the ambient noise. However, the sodar can be replaced by a ship motion-corrected Doppler lidar (Achtert et al., 2015). Likewise, the surface turbulence fluxes can also be made on board after careful correction for flow distortion around the ship and for its motions (e.g., Prytherch et al., 2015, 2017). It should therefore be possible to equip research icebreakers and other ships navigating in the Arctic with instruments that would provide similar information on a quasi-routine basis.

#### Acknowledgments

ASCOS was made possible by funding from the Knut and Alice Wallenberg Foundation and the DAMOCLES European Union 6th Framework Program Integrated Research Project. The Swedish Polar Research Secretariat (SPRS) provided access to the icebreaker *Oden* and logistical support. We are grateful to the SPRS logistical staff and to *Oden's* Captain Mattias Peterson and his crew. ASCOS is an IPY project under the AICIA-IPY umbrella and an endorsed SOLAS project. I.M.B., B.J.B., C.E.B., G.C., and R.A.A. were funded by NERC grants NE/E010008/1, NE/H02168X/1, and NE/I028858/1; C.E.B. was partly funded by the UK Met Office. P.O.G.P. and M.D.S. were supported by the NSF (ARC1023366, ARC1203902) and U.S. Department of Energy (DE-SC0007005, DE-SC0011918). The cloud radar, scanning radiometer, microwave radiometer, and wind profiler were provided by NOAA; the radiosounding system by the Finnish Meteorological Institute; and the sodar and tethered balloon by the UK National Centre for Atmospheric Science (NCAS) Atmospheric Measurement Facility. ASCOS data are archived at the Bolin Centre for Climate Research and available from <http://bolin.su.se/data/ascos/>.

#### References

- Achtert, P., Brooks, I. M., Brooks, B. J., Moat, B. I., Prytherch, J., Persson, P. O. G., & Tjernström, M. (2015). Measurement of wind profiles over the Arctic Ocean from ship-borne Doppler lidar. *Atmospheric Measurement Techniques*, 8, 4993–5007. <https://doi.org/10.5194/amt-8-4993-2015>
- Andreas, E. L., Horst, T. W., Grachev, A. A., Persson, P. O. G., Fairall, C. W., Guest, P. S., & Jordan, R. E. (2010). Parameterising turbulent exchange over summer sea ice and the marginal ice zone. *Quarterly Journal of the Royal Meteorological Society*, 136B, 927–943. <https://doi.org/10.1002/qj.618>
- Andreas, E. L., Jordan, R. E., & Makshatas, A. P. (2005). Parameterizing turbulent exchange over sea ice: The Ice Station Weddel results. *Boundary-Layer Meteorology*, 114, 439–460. <https://doi.org/10.1007/s10546-004-1414-7>
- Balsley, B. B., Svensson, G., & Tjernström, M. (2008). On the scale-dependence of the gradient Richardson number in the residual layer. *Boundary-Layer Meteorology*, 127, 57–72. <https://doi.org/10.1007/s10546-007-9251-0>
- Banta, R., Pechugina, Y., & Newsom, R. (2003). Relationship between low-level jet properties and turbulence kinetic energy in the nocturnal stable boundary layer. *Journal of the Atmospheric Sciences*, 60, 2549–2555. [https://doi.org/10.1175/1520-0469\(2003\)060<2549:RBLJPA>2.0.CO;2](https://doi.org/10.1175/1520-0469(2003)060<2549:RBLJPA>2.0.CO;2)
- Bintanja, R., Graverson, R. G., & Hazeleger, W. (2011). Arctic winter warming amplified by the thermal inversion and consequent low infrared cooling to space. *Nature Geoscience*, 4, 758–761. <https://doi.org/10.1038/NGEO1285>
- Bintanja, R., van der Linden, E. C., & Hazeleger, W. (2012). Boundary layer stability and Arctic climate change: A feedback study using EC-Earth. *Climate Dynamics*, 39, 2659–2673. <https://doi.org/10.1007/s00382-011-1272-1>
- Birch, C. E., Brooks, I. M., Tjernström, M., Milton, S. F., Earnshaw, P., Söderberg, S., & Persson, P. O. G. (2009). The performance of a global and mesoscale model over the central Arctic Ocean during late summer. *Journal of Geophysical Research*, 114, D13104. <https://doi.org/10.1029/2008JD010790>
- Birch, C. E., Brooks, I. M., Tjernström, M., Shupe, M., Milton, S. F., Earnshaw, P., ... Leck, C. (2012). Modelling atmospheric structure, cloud and their response to CCN in the central Arctic: ASCOS case studies. *Atmospheric Chemistry and Physics*, 12, 3419–3435. <https://doi.org/10.5194/acp-12-3419-2012>
- Blackadar, A. K., & Tennekes, H. (1968). Asymptotic similarity in neutral barotropic planetary boundary layers. *Journal of the Atmospheric Sciences*, 25, 1015–1020. [https://doi.org/10.1175/1520-0469\(1968\)025<1015:ASINBP>2.0.CO;2](https://doi.org/10.1175/1520-0469(1968)025<1015:ASINBP>2.0.CO;2)
- Chandrasekhar, S. (1961). *Hydrodynamic and Hydromagnetic Stability* (pp. 652). Oxford, UK: Clarendon Press.
- Curry, J. A. (1986). Interactions among turbulence, radiation and microphysics in Arctic stratus clouds. *Journal of the Atmospheric Sciences*, 43, 90–106. [https://doi.org/10.1175/1520-0469\(1986\)043<0090:IATRAM>2.0.CO;2](https://doi.org/10.1175/1520-0469(1986)043<0090:IATRAM>2.0.CO;2)
- Curry, J. A., & Ebert, E. E. (1992). Annual cycle of radiative fluxes over the Arctic Ocean: Sensitivity to cloud optical properties. *Journal of Climate*, 5, 1267–1280. [https://doi.org/10.1175/1520-0442\(1992\)005<1267:ACORFO>2.0.CO;2](https://doi.org/10.1175/1520-0442(1992)005<1267:ACORFO>2.0.CO;2)

- Curry, J. A., Hobbs, P. V., King, M. D., Randall, D. A., Minnis, P., Isaac, G. A., ... Wylie, D. (2000). FIRE Arctic Clouds Experiment. *Bulletin of the American Meteorological Society*, 81, 5–30. [https://doi.org/10.1175/1520-0477\(2000\)081<0005:FACE>2.3.CO;2](https://doi.org/10.1175/1520-0477(2000)081<0005:FACE>2.3.CO;2)
- Deusebio, E., Vallgren, A., & Lindborg, E. (2013). The route to dissipation in strongly stratified and rotating flows. *Journal of Fluid Mechanics*, 720, 66–103. <https://doi.org/10.1017/jfm.2012.611>
- Durrán, D. R., & Klemp, J. B. (1982). On the effects of moisture on the Brunt-Väisälä frequency. *Journal of the Atmospheric Sciences*, 39, 2152–2158. [https://doi.org/10.1175/1520-0469\(1982\)039<2152:OTEOMO>2.0.CO;2](https://doi.org/10.1175/1520-0469(1982)039<2152:OTEOMO>2.0.CO;2)
- Edwards, J. M., & Slingo, A. (1996). Studies with a flexible new radiation code. Part I. Choosing a configuration for a large-scale model. *Quarterly Journal of the Royal Meteorological Society*, 122, 689–719. <https://doi.org/10.1002/qj.49712253107>
- Elvidge, A. D., Renfrew, I. A., Weiss, A. I., Brooks, I. M., Lachlan-Cope, T. A., & King, J. C. (2016). Observations of surface momentum exchange over the marginal-ice-zone and recommendations for its parameterization. *Atmospheric Chemistry and Physics*, 16, 1545–1563. <https://doi.org/10.5194/acp-16-1545-2016>
- Garratt, J. R. (1992). *The Atmospheric Boundary Layer. Cambridge atmospheric and space science series* (pp. 316). Cambridge, UK: Cambridge Univ. Press.
- Gossard, E. E., Gaynor, J. E., Zamora, R. J., & Neff, W. D. (1985). Fine structure of elevated stable layers observed by sounder and in situ tower sensors. *Journal of the Atmospheric Sciences*, 42, 2156–2169. [https://doi.org/10.1175/1520-0469\(1985\)042<2156:FOESLO>2.0.CO;2](https://doi.org/10.1175/1520-0469(1985)042<2156:FOESLO>2.0.CO;2)
- Held, A., Brooks, I. M., Leck, C., & Tjernström, M. (2011). On the potential contribution of open lead particle emissions to the central Arctic aerosol concentration. *Atmospheric Chemistry and Physics*, 11, 3093–3105. <https://doi.org/10.5194/acp-11-3093-2011>
- Igel, A. L., Ekman, A. M. L., Leck, C., Tjernström, M., Savre, J., & Sedlar, J. (2017). The free troposphere as a potential source of arctic boundary layer aerosol particles. *Geophysical Research Letters*, 44, 7053–7060. <https://doi.org/10.1002/2017GL073808>
- Ingram, W. J., Woodward, S., & Edwards, J. M. (1997). Radiation. UM Documentation Paper No 23. UK Met Office, Exeter, UK.
- Intrieri, J. M., Fairall, C. W., Shupe, M. D., Persson, P. O. G., Andreas, E. L., Guest, P. S., Moritz, R. E. (2002). An annual cycle of Arctic surface cloud forcing at SHEBA. *Journal of Geophysical Research*, 107(C10), 8039. <https://doi.org/10.1029/2000JC000439>
- Liu, Y., & Key, J. R. (2016). Assessment of Arctic cloud cover anomalies in atmospheric reanalysis products using satellite data. *Journal of Climate*, 29, 6065–6083. <https://doi.org/10.1175/JCLI-D-15-0861.1>
- Kaimal, J. C., & Finnigan, J. J. (1994). *Atmospheric boundary layer flows: Their structure and measurement*, Oxford, UK: Oxford University Press.
- Mauritsen, T., & Svensson, G. (2007). Observations of stably stratified shear-driven atmospheric turbulence at low and high Richardson numbers. *Journal of the Atmospheric Sciences*, 64, 645–655. <https://doi.org/10.1175/JAS3856.1>
- Meillier, Y. (2004). Periodic modulation of fine-scale turbulence by gravity waves above the nocturnal boundary layer: Experimental validation using in situ measurements, PhD Thesis, 145 pp, Univ. of Colorado, Boulder, Colorado.
- Meillier, Y. (2008). Modulation of small-scale turbulence by gravity waves in the nocturnal boundary layer. *Journal of the Atmospheric Sciences*, 65, 1414–1427. <https://doi.org/10.1175/2007JAS2359.1>
- Miles, J. W. (1961). On the stability of heterogeneous shear flow. *Journal of Fluid Mechanics*, 10, 496–508.
- Nastrom, G. D., & Gage, K. S. (1985). A climatology of atmospheric wave number spectra of wind and temperature observed by commercial aircraft. *Journal of the Atmospheric Sciences*, 42, 950–960. [https://doi.org/10.1175/1520-0469\(1985\)042<0950:ACOAWS>2.0.CO;2](https://doi.org/10.1175/1520-0469(1985)042<0950:ACOAWS>2.0.CO;2)
- Nilsson, E. D. (1996). Planetary boundary layer structure and air mass transport during the International Arctic Ocean Expedition 1991. *Tellus*, 48B, 178–196. <https://doi.org/10.1034/j.1600-0889.1996.t01-1-00004.x>
- Overland, J. E. (1985). Atmospheric boundary layer structure and drag coefficients over sea ice. *Journal of Geophysical Research*, 90, 9029–9049. <https://doi.org/10.1029/JC090iC05p09029>
- Persson, P. O. G. (2012). Onset and end of the summer melt season over sea ice: Thermal structure and surface energy perspective from SHEBA. *Climate Dynamics*, 39, 1349–1371. <https://doi.org/10.1007/s00382-011-1196-9>
- Persson, P. O. G., Fairall, C. W., Andreas, E. L., Guest, P. S., & Perovich, D. K. (2002). Measurements near the Atmospheric Surface Flux Group tower at SHEBA: Near-surface conditions and surface energy budget. *Journal of Geophysical Research*, 107(C10), 8045. <https://doi.org/10.1029/2000JC000705>
- Pithan, F., Medeiros, B., & Mauritsen, T. (2014). Mixed-phase clouds cause climate model biases in Arctic wintertime temperature inversions. *Climate Dynamics*, 43, 289–303. <https://doi.org/10.1007/s00382-013-1964-9>
- Prytherch, J., Brooks, I. M., Crill, P., Thornton, B., Salisbury, D. J., Tjernström, M., ... Humborg, C. (2017). Direct determination of the air-sea CO<sub>2</sub> gas transfer velocity in Arctic sea ice regions. *Geophysical Research Letters*, 44, 3770–3778. <https://doi.org/10.1002/2017GL073593>
- Prytherch, J., Yelland, M. J., Brooks, I. M., Tupman, D. J., Pascal, R. W., Moat, B. I., & Norris, S. J. (2015). Motion-correlated flow distortion and wave-induced biases in air-sea flux measurements from ships. *Atmospheric Chemistry and Physics*, 15, 10,619–10,629. <https://doi.org/10.5194/acp-15-10619-2015>
- Rohr, J. J., Itsweire, E., Helland, K., & van Atta, C. W. (1988). Growth and decay of turbulence in a stably stratified shear flow. *Journal of Fluid Mechanics*, 195, 77–111.
- Sedlar, J. (2014). Implications of limited liquid water path on static mixing within Arctic low-level clouds. *Journal of Applied Meteorology and Climatology*, 53, 2775–2789. <https://doi.org/10.1175/JAMC-D-14-0065.1>
- Sedlar, J., & Shupe, M. D. (2014). Characteristic nature of vertical motions observed in Arctic mixed-phase stratocumulus. *Atmospheric Chemistry and Physics*, 14, 3461–3478. <https://doi.org/10.5194/acp-14-3461-2014>
- Sedlar, J., Shupe, M. D., & Tjernström, M. (2012). On the relationship between thermodynamic structure and cloud top, and its climate significance in the Arctic. *Journal of Climate*, 25, 2374–2393. <https://doi.org/10.1175/JCLI-D-11-00186.1>
- Sedlar, J., Tjernström, M., Mauritsen, T., Brooks, I. M., Birch, C. E., Shupe, M., ... Leck, C. (2011). A transitioning Arctic surface energy budget: The impacts of solar zenith angle, surface albedo and cloud radiative forcing. *Climate Dynamics*, 37, 1643–1660. <https://doi.org/10.1007/s00382-010-0937-5>
- Shupe, M. D. (2007). A ground-based multiple remote-sensor cloud phase classifier. *Geophysical Research Letters*, 34, L22809. <https://doi.org/10.1029/2007GL031008>
- Shupe, M. D., Brooks, I. M., & Canut, G. (2012). Evaluation of turbulent dissipation rate retrievals from Doppler cloud radar. *Atmospheric Measurement Techniques*, 5, 1375–1385. <https://doi.org/10.5194/amt-5-1375-2012>
- Shupe, M. D., & Intrieri, J. M. (2004). Cloud radiative forcing of the Arctic surface: The influence of cloud properties, surface albedo, and solar zenith angle. *Journal of Climate*, 17, 616–628. [https://doi.org/10.1175/1520-0442\(2004\)017<0616:CRFOTA>2.0.CO;2](https://doi.org/10.1175/1520-0442(2004)017<0616:CRFOTA>2.0.CO;2)
- Shupe, M. D., Persson, P. O. G., Brooks, I. M., Tjernström, M., Sedlar, J., Mauritsen, T., ... Sjogren, S. (2013). Cloud and boundary layer interactions over the Arctic sea-ice in late summer. *Atmospheric Chemistry and Physics*, 13, 9379–9400. <https://doi.org/10.5194/acp-13-9379-2013>
- Shupe, M. D., Turner, D. D., Zwink, A., Theiman, M. M., Mlawer, M. J., & Shippert, T. R. (2015). Deriving Arctic cloud microphysics at Barrow: Algorithms, results, and radiative closure. *Journal of Applied Meteorology and Climatology*, 54, 1675–1689. <https://doi.org/10.1175/JAMC-D-15-0054.1>

- Shupe, M. D., Walden, V. P., Eloranta, E., Uttal, T., Campbell, J. R., Starkweather, S. M., & Shiobara, M. (2011). Clouds at Arctic atmospheric observatories. Part I: Occurrence and macrophysical properties. *Journal of Applied Meteorology and Climatology*, *50*, 626–644. <https://doi.org/10.1175/2010JAMC2467.1>
- Solomon, A., Shupe, M. D., Persson, P. O. G., & Morrison, H. (2011). Moisture and dynamical interactions maintaining decoupled Arctic mixed-phase stratocumulus in the presence of a humidity inversion. *Atmospheric Chemistry and Physics*, *11*, 10,127–10,148. <https://doi.org/10.5194/acp-11-10127-2011>
- Solomon, A. S., Shupe, M. D., Persson, P. O. G., Morrison, H., Yamaguchi, T., Caldwell, P. M., & de Boer, G. (2014). The sensitivity of springtime Arctic mixed-phase stratocumulus clouds to surface layer and cloud-top inversion layer moisture sources. *Journal of the Atmospheric Sciences*, *71*, 574–595. <https://doi.org/10.1175/JAS-D-13-0179.1>
- Sotiropoulou, G., Sedlar, J., Forbes, R., & Tjernström, M. (2016). Summer Arctic clouds in the ECMWF forecast model: An evaluation of cloud parameterization schemes. *Quarterly Journal of the Royal Meteorological Society*, *142*, 387–400. <https://doi.org/10.1002/qj.2658>
- Sotiropoulou, G., Sedlar, J., Tjernström, M., Shupe, M., Brooks, I. M., & Persson, P. O. G. (2014). The thermodynamic structure of summer Arctic stratocumulus and the dynamic coupling to the surface. *Atmospheric Chemistry and Physics*, *14*, 12,573–12,592. <https://doi.org/10.5194/acp-14-12573-2014>
- Stephens, G. L. (1978). Radiation profiles in extended water clouds. II: Parameterization schemes. *Journal of the Atmospheric Sciences*, *35*, 2123–2132. [https://doi.org/10.1175/1520-0469\(1978\)035<2123:RPIEWC>2.0.CO;2](https://doi.org/10.1175/1520-0469(1978)035<2123:RPIEWC>2.0.CO;2)
- Stull, R. B. (1988). *Introduction to Boundary Layer Meteorology* (pp. 666). Dordrecht, The Netherlands: Kluwer Academic Publishers.
- Tjernström, M. (2005). The summer Arctic boundary layer during the Arctic Ocean Experiment 2001 (AOE-2001). *Boundary-Layer Meteorology*, *117*, 5–36. <https://doi.org/10.1007/s10546-004-5641-8>
- Tjernström, M., Balsley, B. B., Svensson, G., & Nappo, C. J. (2009). The effects of critical layers on residual layer turbulence. *Journal of the Atmospheric Sciences*, *66*, 468–480. <https://doi.org/10.1175/2008JAS2729.1>
- Tjernström, M., Birch, C. E., Brooks, I. M., Shupe, M. D., Persson, P. O. G., Sedlar, J., ... Wheeler, C. R. (2012). Meteorological conditions in the central Arctic summer during the Arctic Summer Cloud Ocean Study (ASCOS). *Atmospheric Chemistry and Physics*, *12*, 6863–6889. <https://doi.org/10.5194/acp-12-6863-2012>
- Tjernström, M., & Graversen, R. G. (2009). The vertical structure of the lower Arctic troposphere analysed from observations and ERA-40 reanalysis. *Quarterly Journal of the Royal Meteorological Society*, *135*, 431–433. <https://doi.org/10.1002/qj.380>
- Tjernström, M., Leck, C., Birch, C. E., Bottenheim, J. W., Brooks, B. J., Brooks, I. M., ... Wheeler, C. R. (2014). The Arctic Summer Cloud-Ocean Study (ASCOS): Overview and experimental design. *Atmospheric Chemistry and Physics*, *14*, 2823–2869. <https://doi.org/10.5194/acp-14-2823-2014>
- Tjernström, M., Sedlar, J., & Shupe, M. D. (2008). How well do regional climate models reproduce radiation & clouds in the Arctic? *Journal of Applied Meteorology and Climatology*, *47*, 2405–2422. <https://doi.org/10.1175/2008JAMC1845.1>
- Tjernström, M., Shupe, M. D., Brooks, I. M., Persson, P. O. G., Prytherch, J., Salisbury, D. J., ... Wolfe, D. (2015). Warm-air advection, air mass transformation and fog causes rapid ice melt. *Geophysical Research Letters*, *42*, 5594–5602. <https://doi.org/10.1002/2015GL064373>
- Tjernström, M., Zagar, M., Svensson, G., Cassano, J. C., Pfeifer, S., Rinke, A., ... Shaw, M. (2005). Modelling the Arctic boundary layer: An evaluation of six ARCMIP regional-scale models using data from the SHEBA project. *Boundary-Layer Meteorology*, *117*, 337–381. <https://doi.org/10.1007/s10546-004-7954-z>
- Vihma, T., Pirazzini, R., Fer, I., Renfrew, I. A., Sedlar, J., Tjernström, M., ... Gascar, J. C. (2014). Advances in understanding and parameterization of small-scale physical processes in the marine Arctic climate system: A review. *Atmospheric Chemistry and Physics*, *14*, 9403–9450. <https://doi.org/10.5194/acp-14-9403-2014>
- Wang, X., & Key, J. R. (2004). Arctic surface, cloud, and radiation properties based on the AVHRR polar pathfinder dataset. Part I: Spatial and temporal characteristics. *Journal of Climate*, *18*, 2558–2574. <https://doi.org/10.1175/JCLI3438.1>
- Westwater, E., Han, Y., Irisov, V. G., Leuskiy, V., Kadygrov, E. N., & Viazankin, S. A. (1999). Remote sensing of boundary layer temperature profiles by a scanning 5-mm microwave radiometer and RASS: Comparison experiments. *Journal of Atmospheric and Oceanic Technology*, *16*, 805–818. [https://doi.org/10.1175/1520-0426\(1999\)016<0805:RSOBLT>2.0.CO;2](https://doi.org/10.1175/1520-0426(1999)016<0805:RSOBLT>2.0.CO;2)
- Westwater, E. R., Han, Y., Shupe, M. D., & Matrosov, S. Y. (2001). Analysis of integrated cloud liquid and precipitable water vapor retrievals from microwave radiometers during the Surface Heat Budget of the Arctic Ocean project. *Journal of Geophysical Research*, *106*, 32,019–32,030. <https://doi.org/10.1029/2000JD000055>
- Zilitinkevich, S. S. (2012). The height of the atmospheric planetary boundary layer: State of the art and new development. In H. J. S. Fernando, Z. Klaić, & J. McCulley (Eds.), *National Security and Human Health Implications of Climate Change (NATO Science for Peace and Security Series C: Environmental Security)* (pp. 147–161). Dordrecht: Springer. [https://doi.org/10.1007/978-94-007-2430-3\\_13](https://doi.org/10.1007/978-94-007-2430-3_13)
- Zygmuntowska, M., Mauritsen, T., Quaas, J., & Kaleschke, L. (2012). Arctic clouds and surface radiation—A critical comparison of satellite retrievals and the ERA-Interim reanalysis. *Atmospheric Chemistry and Physics*, *12*, 6667–6677. <https://doi.org/10.5194/acp-12-6667-2012>